Engineering Fracture Mechanics 330 (2025) 111659

Contents lists available at ScienceDirect

Engineering Fracture Mechanics

journal homepage: www.elsevier.com/locate/engfracmech

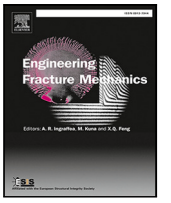

Micromechanical modelling of stress corrosion cracking in PEO-coated biodegradable magnesium alloys using multiphysics phase-field method

Dawei Zhang [a], Songyun Ma [a,*], Cheng Luo [b], Huang Yuan [b], Bernd Markert [a]

[a] Institute of General Mechanics, RWTH Aachen University, Aachen, Germany
[b] School of Aerospace Engineering, Tsinghua University, Beijing, PR China

ARTICLE INFO

Keywords:
Biodegradable magnesium alloys
Stress corrosion cracking
Phase-field method
PEO coating
Hydrogen embrittlement

ABSTRACT

Plasma electrolytic oxidation (PEO) coatings have been developed to regulate the degradation behaviour of biomedical magnesium alloy implants in physiological environments. However, accurately quantifying the stress corrosion cracking (SCC) behaviour of PEO-coated magnesium alloys remains challenging in both *in vitro* and *in vivo* conditions. To tailor and optimise the implant performance under complex chemo-mechanical loading conditions, it is essential to develop computational models to elucidate the SCC process in PEO-coated biodegradable magnesium alloys. In this study, we present a multiphysics phase-field model to capture the interactions among corrosion, fracture, and hydrogen diffusion associated with the SCC phenomena. The proposed model incorporates displacement field, fracture field, corrosion field, magnesium concentration field, and hydrogen concentration field as global primary variables. Three numerical examples are employed to (i) examine the influence of hydrogen embrittlement on the SCC behaviour of magnesium alloys, (ii) validate the model by comparing with *in vitro* experiments of a PEO-coated medical-grade magnesium alloy WE43MEO, and (iii) numerically investigate the SCC behaviour of PEO-coated magnesium alloys with post sealing treatments. The results demonstrate that the proposed model can be used as a promising tool for analysing and evaluating the SCC susceptibility of PEO-coated magnesium alloys in biomedical applications.

1. Introduction

Biodegradable magnesium alloys represent a revolutionary class of next-generation biomedical materials for orthopedic implants, combining exceptional mechanical performance and biocompatibility. The resorption of biodegradable magnesium alloys within human body eliminates the need of follow-up removal surgeries, significantly reducing patient risks and alleviating substantial socioeconomic burdens on healthcare systems. However, the fast corrosion rate of magnesium alloys in physiological environments leads to a critical challenge for their biomedical applications [1]. In this context, various surface-modification techniques have been developed to reduce the surface activity of biodegradable magnesium alloys, aiming to achieve a desirable corrosion rate [2–4]. Among these surface modification methods, plasma electrolytic oxidation (PEO) has garnered significant attention for its versatility, cost-effectiveness, and environmental friendliness [5]. However, the MgO-based ceramic coatings produced through PEO are generally porous structures and contain numerous microdefects [6]. These defects facilitate the penetration of electrolytes towards

* Corresponding author.
E-mail address: ma@iam.rwth-aachen.de (S. Ma).

https://doi.org/10.1016/j.engfracmech.2025.111659
Received 5 June 2025; Received in revised form 16 October 2025; Accepted 27 October 2025
Available online 30 October 2025

the alloy substrate during immersion, thereby diminishing the protective effectiveness of the coatings. This issue is particularly amplified under external mechanical loadings, further compromising the coatings' performance.

Biodegradable magnesium alloy implants face the risk of stress corrosion cracking (SCC) due to the combined effects of a corrosive physiological environment and daily physical activities, often leading to premature failure. Two mechanisms dominate the occurrence of SCC in magnesium alloys: (1) anodic dissolution mechanism, where the crack continues to expand at locally ruptured passive film sites under the action of stress [7,8]; (2) hydrogen embrittlement, where atomic hydrogen produced by electrochemical corrosion infiltrates the Mg matrix, weakening its mechanical strength [9,10]. Depending on materials and corrosion environments, either mechanism can predominate, or both can act concurrently [11]. Notably, *in vitro* experiments have indicated that both mechanisms influence the SCC behaviour of WE43 magnesium alloys in simulated body fluids [12,13]. Although the corrosion resistance of biodegradable magnesium alloys has been widely studied and improved by PEO coatings without mechanical loadings [14–16], their effectiveness in offering a better SCC resistance under chemomechanical loadings should be systematically investigated for biomedical applications [17].

To this end, many *in vitro* experimental studies have been contributed to understand the effect of PEO coatings on the SCC behaviour of magnesium alloys. Srinivasan et al. [7,17,18] evaluated the SCC behaviour of PEO-coated AM50 and AZ61 magnesium alloys in ASTM D1384 solution using slow strain rate tensile (SSRT) tests. It was observed that PEO coatings enhanced SCC resistance in AM50, while they were less effective for AZ61 at very low strain rates (1×10^{-7} s^{-1}). Similarly, Xiong et al. [19] reported that PEO-coated AZ80 magnesium alloy exhibited an ultimate tensile strength comparable to uncoated specimens under a loading rate of 5.3×10^{-7} s^{-1} in simulated body fluids (SBFs). Meanwhile, He et al. [20] found that PEO-coated AZ31 magnesium alloys in NaCl solution exhibited a fracture strain similar to uncoated samples, but a significantly higher ultimate tensile strength under SSRT conditions. Daavari et al. [21] also conducted SSRT tests on PEO-coated AZ31B magnesium alloys in SBFs, demonstrating that PEO coatings markedly improve the fracture strain and ultimate tensile strength in AZ31B magnesium alloys. Nachtsheim et al. [22] reported that the PEO-coated and uncoated magnesium alloy WE43MEO exhibited no significant differences in the ultimate tensile strength during static *in vitro* corrosion tests in the organic Dulbecco's modified Eagles' medium (DMEM) with different stress levels. These findings reveal that both the magnesium alloy substrate and the chemomechanical loadings conditions affect the SCC resistance of PEO-coated Mg implants [11]. Therefore, it is of imperative importance to gain a more physical understanding into the SCC mechanism in biodegradable magnesium alloys with PEO coatings.

For this purpose, numerous efforts have been devoted into developing both phenomenological and physics-based computational models to predict the SCC behaviour of biodegradable magnesium alloys, including continuum damage mechanics (CDM) models, peridynamics (PD) models and phase-field models. Gastaldi et al. [23] developed a CDM model to simulate the degradation process of bioabsorbable Mg stents accounting for uniform corrosion and stress corrosion. Although the CDM-based phenomenological model can describe the damage process by introducing different damage evolution laws for distinct damage mechanisms [24,25], it lacks a comprehensive physical explanation for the electrochemical–mechanical coupling phenomena of SCC. De Meo et al. [26] proposed a PD model for the hydrogen-assisted corrosion cracking based on the adsorption-induced decohesion mechanism. Recently, a fully coupled fracture-corrosion PD model was proposed by Chen et al. [27] to capture the pit-to-crack transition phenomena by neglecting the diffusion of species. However, the applications of PD models is limited by the high computational complexity and difficulties in the treatment of boundary conditions [28]. Phase-field method has emerged as a promising and flexible approach for modelling interface movement and crack propagation. In the past few years, it has been developed for modelling stress corrosion cracking in biodegradable magnesium alloys. Xie et al. [29] built a multiphase-field model for considering the interplay between electric field, corrosion and stress in biodegradable magnesium alloys at the micro-scale. Kovacevic et al. [30] introduced a phase-field model that accounts for the synergistic effects of an aggressive environment and mechanical loading in accelerating the corrosion kinetics of magnesium alloys. Zhang et al. [31] proposed a fully coupled fracture-corrosion phase-field model for modelling the SCC behaviour of biodegradable magnesium alloys and validated the phase-field simulations with *in vitro* experiments. However, these phase-field models neglect the effect of hydrogen in the SCC behaviour in biodegradable magnesium alloys. This implies that the presented computational models cannot accurately capture the multiphysics interactions in the SCC process of biodegradable magnesium alloys.

Besides the deformation-fracture-corrosion interaction in alloy substrates, the complex microstructures of PEO coatings significantly affect the SCC behaviour of the alloy matrix. Cui et al. [15] found that the PEO coating thickness and porosity have a significant influence on the degradation of biodegradable magnesium alloys. Němcová et al. [32] showed that stress concentration caused by the roughness of coating/substrate interface results in earlier fatigue crack initiation in corrosive environment. Therefore, it is important to correlate the porous microstructural features of PEO coatings and the associated SCC behaviour of magnesium alloys. Gazenbiller et al. [33] proposed a macroscopic damage model to quantify the effect of PEO coating's microstructure on the mechanical response of magnesium alloys at slow strain rates. Van Gaalen et al. [34] developed experimental and computational methods to evaluate the influence of PEO surface treatments on the corrosion process of a medical-grade magnesium alloy WE43MEO. Ma et al. [35] developed a phase-field-based machine-learning model to predict the long-term corrosion behaviour of biodegradable magnesium alloys with different coating microstructures. However, these computational models cannot capture the effect of the microstructural defects of PEO coatings on the strongly coupled corrosion and fracture behaviours, resulting in the necessity to develop micromechanical models for assessing the mechanical performance of PEO-coated magnesium alloys in corrosive environments.

The present work is devoted to developing a multiphysics phase-field model that captures the complex mechanisms governing the SCC behaviour of biodegradable magnesium alloys. The thermodynamically consistent phase-field SCC model enables a unified simulation of corrosion, fracture, and hydrogen diffusion on the degradation of PEO-coated biomedical magnesium alloys. To the best

Nomenclature

Symbol	Description
A	Curvature of the magnesium chemical free energy density
$\boldsymbol{b}_{\mathrm{f}}$	External body force
b	Evolution coefficient of diffusivity in coating's microdefects
$\mathbb{C}$	Fourth-order symmetric elasticity tensor
c_{M}, c_{M}^{*}	Magnesium concentration field and normalised magnesium concentration field
c_{S}^{*}, c_{L}^{*}	Normalised magnesium concentration in metal phase and corrosion phase
c_{H}	Hydrogen concentration field
c_{H0}	Reference hydrogen concentration
c_{solid}	Saturated magnesium concentration in alloy
c_{Le}^{*}	Normalised saturated magnesium concentration in corroded material
D, $\mathcal{D}$	Dissipation energy and dissipation energy density
D_{Mp}, D_{Ml}	Diffusion coefficient of magnesium in corrosion product and electrolyte
D_{Hp}, D_{Hl}	Diffusion coefficient of hydrogen in alloy and electrolyte
$\mathfrak{e}$	Specific internal energy
$\mathfrak{e}_{\mathrm{M}}^{\mathrm{f}}$, $\mathfrak{e}_{\mathrm{H}}^{\mathrm{f}}$	Specific enthalpy supply of magnesium flux and hydrogen flux
f_{d}, f_{p}	Fracture threshold function and yield function
$\bar{G}$	Effective shear constant
g_{d}, g_{dm}, g_{dc}	Critical fracture energy of corroded material, uncorroded, and totally corroded material
g_{dm0}, $g_{\mathrm{dm}\infty}$	Initial and degraded critical fracture energy of uncorroded material
g_{w}	Chemical double well potential of corrosion
$\bar{H}$	Effective hardening modulus
$\mathcal{H}$	Historical maximum driving force for the crack field
h_{d}, h_{dc}, h_{dh}	Fracture, corrosion and hydrogen degradation function
h_{c}, h_{f}	Interpolation function of chemical free energy and diffusion mobility
$\boldsymbol{h}_{\mathrm{H}}$, $\boldsymbol{h}_{\mathrm{M}}$	Hydrogen and magnesium flux
$\boldsymbol{I}$	Second-order identity tensor
$\bar{K}$	Effective bulk modulus
l_{d}	Fracture interface thickness
$L_{\phi_{\mathrm{c}}}$	Corrosion interface kinetics coefficient
$\mathcal{L}_{\mathrm{p}}$, $\mathcal{L}_{\mathrm{d}}$	Plastic and fracture Lagrange functional
m_{c}, m_{d}, m_{p}	Corrosion, fracture and plasticity coupling parameter
M_{H}, M_{Mg}	Diffusion mobility of hydrogen and magnesium
N	Density of lattice sites of magnesium alloys
$\boldsymbol{q}$	Heat flux
r	Heat source
R	Gas constant
$\mathfrak{s}$	Specific internal entropy
$\mathfrak{s}_{\mathrm{M}}^{\mathrm{f}}$, $\mathfrak{s}_{\mathrm{H}}^{\mathrm{f}}$	Specific entropy supply of magnesium flux and hydrogen flux
r_{d}, r_{c}	Fracture and corrosion resistance
$\boldsymbol{s}_{\gamma}$, $s_{\phi_{\mathrm{d}}}$, $s_{\phi_{\mathrm{c}}}$, $\boldsymbol{s}_{\mathrm{M}}$, $\boldsymbol{s}_{\mathrm{H}}$	Dissipative force of plasticity, fracture, corrosion, magnesium diffusion and hydrogen diffusion
t	Time
$\boldsymbol{t}_{\mathrm{f}}$	Surface traction force
T	Temperature
t_{M}, t_{H}	Microtraction associated with c_{M} and c_{H}
υ	Corrosion dissipation potential functional
$\bar{V}_{\mathrm{H}}$	Partial molar volume of hydrogen in magnesium alloys
W_{int}, W_{ext}	Internal and external energy
w_{c}	Height of the double-well energy barrier
w_{M}, w_{H}	Sclar microforce associated with c_{M} and c_{H}
α_{c}	Gradient energy coefficient of the corrosion phase field
χ	Fracture surface density function
$\Delta g_{\mathrm{b}}^{0}$	Gibbs free energy difference for hydrogen embrittlement
ε	Strain tensor
ε_{S}, ε_{D}, $\varepsilon_{\mathrm{D}}^{\mathrm{e}}$, $\varepsilon_{\mathrm{D}}^{\mathrm{p}}$	Spherical part, deviatoric part, elastic deviatoric part and plastic deviatoric part of the strain tensor

ε^{e}, ε^{p}	Elastic and plastic strain tensor
η	Occupancy of hydrogen in lattice sites
γ	Equivalent plastic strain
γ_{crit}	Critical equivalent plastic strain
κ_{M}, κ_{H}	Gradient energy coefficient for magnesium and hydrogen concentration
Λ	Hydrogen damage coefficient
λ_d, λ_p	Fracture and plastic Lagrange multiplier
μ_{M}, μ_{H}	Chemical potential of magnesium and hydrogen
$\tilde{\mu}_{M}$, $\tilde{\mu}_{H}$	Net chemical potential of magnesium and hydrogen
Ω	Mixing domain
ϕ_{d}, ϕ_{c}	Fracture and corrosion phase-field variable
ψ, ψ^{ch}, ψ^{el}, ψ^{hard}	Total free energy density; chemical, elastic and hardening free energy density
ψ^{ch}_{grad}, ψ^{M}_{bulk}, ψ^{H}_{bulk}	Interfacial, magnesium and hydrogen bulk chemical free energy density
ψ_{S}, ψ_{L}	Magnesium chemical free energy density of metal phase and corrosion phase
ρ	Material density
$\boldsymbol{\sigma}$	Stress tensor
σ_{HS}	Hydrostatic stress
$\bar{\sigma}_y$, σ_{y}	Effective and degraded initial yield stress of materials
$\boldsymbol{\xi}_{M}$, $\boldsymbol{\xi}_{H}$	Vectorial microforce associated with c_{M} and c_{H}
ζ_{dc}, ζ_{pd}	Fracture-corrosion and plastic-fracture coupling force
Abbreviation	**Description**
PEO	Plasma electrolytic oxidation
SCC	Stress corrosion cracking
DMEM	Dulbecoo's modified Eagles' medium
CDM	Continuum damage mechanics
PD	Peridynamics
HEDE	Hydrogen-enhanced decohesion
HELP	Hydrogen-enhanced localised plasticity
ADIE	Hydrogen absorption-induced dislocation emission
DHC	Delayed hydride cracking
SSRT	Slow strain rate tensile
SEM	Scanning electron microscopy

of our knowledge, this is the first study to investigate the SCC behaviour of PEO-coated magnesium alloys using such a multiphysics framework. Furthermore, we conduct computational micromechanical analysis to link the features of microstructural defects in PEO coatings to the SCC behaviour. Three dominant mechanisms in the SCC process of biodegradable magnesium alloys are considered in this study: (i) the transition from magnesium alloys to corrosion products leads to the degradation of fracture toughness; (ii) the cracks in the PEO coating, barrier film and alloy substrate allow the permeation of electrolyte; (iii) the diffusion of hydrogen leads to the hydrogen embrittlement of the alloy substrate. To more deeply understand the SCC mechanism of PEO-coated magnesium alloys, we conduct the computational simulations at the microscopic scale and develop a simplified microstructural model of the coatings based on experimental observations. Using the proposed phase-field model, we numerically analyse the SCC behaviour at the microscale under different mechanical loading conditions, providing a more comprehensive understanding of SCC processes in coated biodegradable magnesium alloys. The developed modelling method provides a new numerical tool to evaluate the SCC behaviour of coated biodegradable magnesium alloys under chemomechanical conditions, which is still an engineering and scientific challenge to advance in silico design and optimisation of coated biodegradable magnesium implants.

The paper is organised as follows. In Section 2, we develop the theoretical formulations of the proposed multiphase-field model within a thermodynamically consistent framework. The role of hydrogen diffusion in the SCC process in biodegradable magnesium alloys is demonstrated in Section 3.1. In Section 3.3, the model is validated by comparing with the experimental results of a PEO-coated medical-grade magnesium alloy WE43MEO under both pure corrosion and static loading-corrosion conditions. The SCC behaviour of the PEO-coated sample after post sealing treatments is studied in Section 3.4. Conclusions and remarks are summarised in Section 4.

2. Theory

In this section, we present the proposed multiphysics phase-field model for describing the corrosion-fracture behaviour of biodegradable magnesium alloys coupled with hydrogen embrittlement. The basic assumptions of the model are stated in Section 2.1. We first introduce kinematic variables in Section 2.2 and mass balance equations in Section 2.3. The force balance equations are derived based on the principle of virtual power in Section 2.4. The thermodynamic consistency is established via free energy imbalance in Section 2.5. The free energy function and the choice of constitutive model are stated in Sections 2.6 and 2.7. The governing equations and boundary conditions are summarised in Section 2.8.

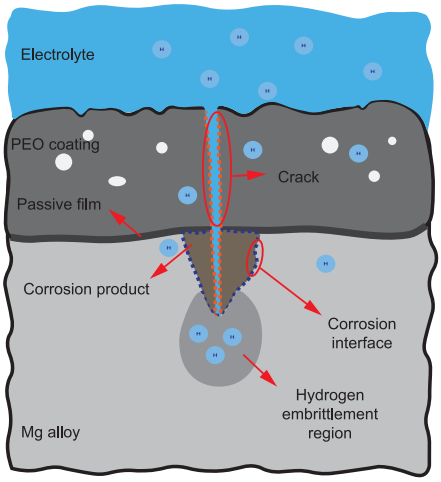

Fig. 1. Schematic illustration of stress corrosion cracking of PEO-coated magnesium alloys in physiological environments.

2.1. Problem outline

In aluminium alloys or stainless steels, relatively stable passive oxide layers are formed on the material surface. The localised breakdown of these layers leads to the development of deep pits [36]. In contrast, Mg alloys generally do not form such stable passive films. Instead, their surface oxides and hydroxides are highly soluble and less protective in physiological conditions. After PEO treatments, a porous ceramic coating and a dense barrier MgO layer are formed on the substrate surface of magnesium alloys, which provides protection to the magnesium alloy matrix against corrosion. However, the microdefects in the PEO coatings enable the permeation of corrosive medium. Meanwhile, if the barrier film is too thin or develops cracks in certain regions, the solution directly contacts the freshly exposed alloy substrate, leading to the localised corrosion [37]. Under *in-vitro* or *in-vivo* conditions, the localised corrosion of Mg alloys is often driven by micro-galvanic interactions between the Mg matrix and intermetallic phases or impurity particles, resulting in shallow and lateral dissolution zones rather than deep and narrow pitting morphology. Furthermore, the ions and organic components continuously react with corrosion products in the long-term corrosion process, promoting the development of a stable corrosion product layer composed of various corrosion byproducts such as $Mg_3(PO_4)_2$ and $Mg_5(CO_3)_4(OH)_25H_2O$. The corrosion products reduce fluid access to the alloy matrix and impede ion transport during long-term corrosion [38]. In this study, we focus on the long-term interaction among deformation, diffusion-controlled corrosion and fracture, and therefore ignore the explicit electrochemical kinetics of complex ion compositions of the electrolyte in the SCC process [31].

According to hydrogen embrittlement theory, hydrogen atoms produced during corrosion can be absorbed and diffuse into magnesium alloys, where their accumulation promotes crack formation [39]. Hydrogen embrittlement is typically categorised into four mechanisms: (i) hydrogen-enhanced decohesion (HEDE), (ii) hydrogen-enhanced localised plasticity (HELP), (iii) hydrogen absorption-induced dislocation emission (AIDE), and (iv) delayed hydride cracking (DHC). In both HEDE and AIDE, the bonding energy between metal atoms is reduced, which can be modelled by lowering the critical fracture energy [40]. The HELP mechanism can be described phenomenologically by making the yield stress a function of hydrogen concentration and plastic strain [41]. Meanwhile, hydride formation in magnesium alloys under SCC conditions can be modelled based on the local solvus [42]. Because these mechanisms often overlap in practice, it can be difficult to pinpoint which one dominates. For simplicity, we neglect the detailed hydrogen–metal reactions and focus solely on modelling the influence of hydrogen on the fracture behaviour.

In summary, the involved coupling mechanisms are assumed as: (i) hydrogen absorption and corrosion reduce the fracture toughness of the material, (ii) cracking in the alloy matrix and corrosion products enhances the diffusivity of magnesium and hydrogen. An overview of the SCC process in PEO-coated magnesium alloys is illustrated in Fig. 1.

2.2. Basic kinematics

We consider a mixing domain of magnesium alloy and electrolyte $\Omega \subset \mathbb{R}^3$ with external boundary $\partial\Omega$, which is decomposed into a solid boundary $\partial\Omega_s$ and an electrolyte boundary $\partial\Omega_l$ with $\partial\Omega = \partial\Omega_s + \partial\Omega_l$ and $\partial\Omega_s \cap \partial\Omega_l = \varnothing$. It is supposed that the electrolyte does not flow but only conducts ions by diffusion. The displacement of the domain is defined by the displacement field $\boldsymbol{u}(\boldsymbol{x}, t)$. Considering the small-strain theory, the strain tensor can be defined as the symmetric part of the spatial gradient of the displacement field:

$$\boldsymbol{\varepsilon} = \nabla_s \boldsymbol{u} = \frac{1}{2}\left(\nabla \boldsymbol{u} + \nabla^T \boldsymbol{u}\right) . \tag{1}$$

$\boldsymbol{\varepsilon}$ is decomposed into its elastic $\boldsymbol{\varepsilon}^e$ and plastic $\boldsymbol{\varepsilon}^{\mathrm{p}}$ parts with $\boldsymbol{\varepsilon} = \boldsymbol{\varepsilon}^{\mathrm{e}} + \boldsymbol{\varepsilon}^{\mathrm{p}}$. The Mg and H concentration states of the domain are defined by the Mg concentration field $c_{\mathrm{M}}(\boldsymbol{x}, t)$ and the hydrogen concentration field $c_{\mathrm{H}}(\boldsymbol{x}, t)$, respectively. Two phase-field variables ϕ_{d} and

ϕ_c are introduced to indicate the fracture and corrosion state of materials. ϕ_d tracks the crack interface in solids with $\phi_d = 0$ for intact material points and $\phi_d = 1$ for completely fractured state. We define $\phi_c = 0$ for the totally corroded material and $\phi_c = 1$ for the uncorroded alloy matrix.

2.3. Balance of mass

Consider an arbitrary domain $\bar{\Omega}$ inside the reference domain Ω, with surface $\partial\bar{\Omega}$. The diffusion of species (Mg ions and hydrogen) across this boundary $\partial\bar{\Omega}$ is accompanied by a change in the species concentration and characterised by a flux. Accordingly, the change rate of the species across $\bar{\Omega}$ is given by

$$\int_{\bar{\Omega}} \dot{c}_M \, dV = -\int_{\partial\bar{\Omega}} \boldsymbol{h}_M \cdot \boldsymbol{n} \, dA \,, \tag{2}$$

and

$$\int_{\bar{\Omega}} \dot{c}_H \, dV = -\int_{\partial\bar{\Omega}} \boldsymbol{h}_H \cdot \boldsymbol{n} \, dA \,. \tag{3}$$

By applying the divergence theorem, the local form of mass balance for Mg ions and hydrogen can be written as

$$\dot{c}_M = -\nabla \cdot \boldsymbol{h}_M \,, \tag{4}$$

and

$$\dot{c}_H = -\nabla \cdot \boldsymbol{h}_H \,. \tag{5}$$

2.4. The principle of virtual power

In consistency with the previously defined kinematics fields, we define a set of rate-like descriptors as $(\dot{\boldsymbol{u}}, \dot{c}_M, \dot{c}_H)$. For their evolution within the domain we associate macroscopic and microscopic force systems. The macroscopic system is defined by: (i) the stress tensor $\boldsymbol{\sigma}$ that expands power over the deformation rate $\dot{\varepsilon}$; (ii) the traction force $\boldsymbol{t}_f$ on the surface with the normal unit vector $\boldsymbol{n}$, that expands power over the velocity $\dot{\boldsymbol{u}}$ on the boundary of the domain, and an external body force $\boldsymbol{b}_f$ that expands power over $\dot{\boldsymbol{u}}$ in the domain.

The microscopic system is defined by: (a) the scalar microforce ω_M that expands power over the Mg concentration change rate $\dot{c}_M$ and the vectorial microforce $\boldsymbol{\xi}_M$ expands power over the Mg concentration gradient $\nabla\dot{c}_M^*$; (b) the scalar microforce ω_H that expands power over the H concentration change rate $\dot{c}_H$ and the vectorial microforce $\boldsymbol{\xi}_H$ expands power over the H concentration gradient $\nabla\dot{c}_H$; (c) the scalar microtraction t_M that expands power over $\dot{c}_M$ on the boundary of the domain; (d) a scalar microtraction t_H that expands power over $\dot{c}_H$ on the boundary of the domain.

For the mixing domain Ω, the internal power $\dot{W}_{int}$ and the external power $\dot{W}_{ext}$ are given by

$$\dot{W}_{int} = \int_{\Omega} \left(\boldsymbol{\sigma} : \dot{\boldsymbol{\varepsilon}} + \omega_M \dot{c}_M + \boldsymbol{\xi}_M \cdot \nabla\dot{c}_M + \omega_H \dot{c}_H + \boldsymbol{\xi}_H \cdot \nabla\dot{c}_H \right) dV \tag{6}$$

and

$$\dot{W}_{ext} = \int_{\Omega} \boldsymbol{b}_f \cdot \dot{\boldsymbol{u}} dV + \int_{\partial\Omega} \left(\boldsymbol{t}_f \cdot \dot{\boldsymbol{u}} + t_M \dot{c}_M + t_H \dot{c}_H \right) dA \,. \tag{7}$$

Assuming that, at arbitrary chosen but fixed time, the fields $(\boldsymbol{u}, c_M, c_H)$ are known, and considering the velocity fields $(\dot{\boldsymbol{u}}, \dot{c}_M, \dot{c}_H)$ and denoting their virtual counterpart by $(\delta\dot{\boldsymbol{u}}, \delta\dot{c}_M, \delta\dot{c}_H)$, we express the virtual powers as

$$\delta\dot{W}_{int} = \int_{\Omega} \left(\boldsymbol{\sigma} : \delta\dot{\boldsymbol{\varepsilon}} + \omega_M \delta\dot{c}_M + \boldsymbol{\xi}_M \cdot \nabla\delta\dot{c}_M + \omega_H \delta\dot{c}_H + \boldsymbol{\xi}_H \cdot \nabla\delta\dot{c}_H \right) dV \,, \tag{8}$$

$$\delta\dot{W}_{ext} = \int_{\Omega} \boldsymbol{b}_f \cdot \delta\dot{\boldsymbol{u}} dV + \int_{\partial\Omega} \left(\boldsymbol{t}_f \cdot \delta\dot{\boldsymbol{u}} + t_M \delta\dot{c}_M + t_H \delta\dot{c}_H \right) dA \,. \tag{9}$$

We proceed to introduce the principle of virtual power, such that

$$\delta\dot{W}_{int} = \delta\dot{W}_{ext} \,. \tag{10}$$

Combining Eqs. (8)–(10) and applying the divergence theorem, the equilibrium equation are obtained as,

$$\begin{aligned} &\int_{\Omega} \left[-\left(\mathrm{div}\boldsymbol{\sigma} + \boldsymbol{b}_f \right) \cdot \delta\dot{\boldsymbol{u}} + \left(\omega_M - \nabla \cdot \boldsymbol{\xi}_M \right) \delta\dot{c}_M + \left(\omega_H - \nabla \cdot \boldsymbol{\xi}_H \right) \delta\dot{c}_H \right] dV \\ &+ \int_{\partial\Omega} \left[\left(\boldsymbol{\sigma}\boldsymbol{n} - \boldsymbol{t}_f \right) \delta\dot{\boldsymbol{u}} + (\boldsymbol{\xi}_M \cdot \boldsymbol{n} - t_M)\delta\dot{c}_M + (\boldsymbol{\xi}_H \cdot \boldsymbol{n} - t_H)\delta\dot{c}_H \right] dA = 0 \end{aligned} \tag{11}$$

leading to the macroscopic and microscopic force balance equations in Ω

$$\mathrm{div}\boldsymbol{\sigma} + \boldsymbol{b}_f = 0 \tag{12}$$

$$\omega_M - \nabla \cdot \boldsymbol{\xi}_M = 0 \tag{13}$$

$$\omega_{\mathrm{H}} - \nabla \cdot \boldsymbol{\xi}_{\mathrm{H}} = 0 \tag{14}$$

and the corresponding force balance on $\partial\Omega$

$$\boldsymbol{\sigma}\boldsymbol{n} = \boldsymbol{t}_{\mathrm{f}} \tag{15}$$

$$\boldsymbol{\xi}_{\mathrm{M}} \cdot \boldsymbol{n} = t_{\mathrm{M}} \tag{16}$$

$$\boldsymbol{\xi}_{\mathrm{H}} \cdot \boldsymbol{n} = t_{\mathrm{H}} \tag{17}$$

2.5. Free energy imbalance

In addition to the mass and force balances introduced above, we impose the restrictions of the first and second laws of thermodynamics through an energy balance and an entropy imbalance [43]. For quasi-static problems, the first law enforces the change rate of the internal energy equal to the supplied external power, which includes contributions from body forces, surface tractions, Mg and H fluxes, as well as thermal fluxes and sources. The second law requires that the change in internal entropy exceed the externally supplied entropy, which arises from species fluxes, thermal fluxes, and thermal sources in our formulation. Letting $\mathfrak{e}$ and $\mathfrak{s}$ denoting the specific internal energy and entropy respectively, the energy balance and entropy inequality read

$$\begin{aligned}\frac{d}{dt}\int_{\Omega}\rho\mathfrak{e}\,dV = &\int_{\Omega}\boldsymbol{b}_{\mathrm{f}}\cdot\dot{\boldsymbol{u}}\,dV + \int_{\partial\Omega}\left(\boldsymbol{t}_{\mathrm{f}}\cdot\dot{\boldsymbol{u}} + t_{\mathrm{M}}\dot{c}_{\mathrm{M}} + t_{\mathrm{H}}\dot{c}_{\mathrm{H}}\right)\,dA \\ &- \int_{\partial\Omega}\left(\mathfrak{e}^{\mathrm{f}}_{\mathrm{M}}\boldsymbol{h}_{\mathrm{M}}\cdot\boldsymbol{n} + \mathfrak{e}^{\mathrm{f}}_{\mathrm{H}}\boldsymbol{h}_{\mathrm{H}}\cdot\boldsymbol{n} + \boldsymbol{q}\cdot\boldsymbol{n}\right)\,dA + \int_{\Omega} r\,dV\,,\end{aligned} \tag{18}$$

$$\frac{d}{dt}\int_{\Omega}\rho\mathfrak{s}\,dV \geq -\int_{\partial\Omega}\left(\mathfrak{s}^{\mathrm{f}}_{\mathrm{M}}\boldsymbol{h}_{\mathrm{M}}\cdot\boldsymbol{n} + \mathfrak{s}^{\mathrm{f}}_{\mathrm{H}}\boldsymbol{h}_{\mathrm{H}}\cdot\boldsymbol{n}\right)\,dA - \int_{\partial\Omega}\frac{\boldsymbol{q}\cdot\boldsymbol{n}}{T}\,dA + \int_{\Omega}\frac{r}{T}\,dV\,, \tag{19}$$

where $\boldsymbol{q}$ is the heat flux, r is a heat source and T is the absolute temperature. $\mathfrak{e}^{\mathrm{f}}_{*}$ and $\mathfrak{s}^{\mathrm{f}}_{*}$ with $*\in\{\mathrm{M},\mathrm{H}\}$ denote the specific enthalpy and entropy provided by a supply of the corresponding specie flux. $\mathfrak{e}^{\mathrm{f}}_{*}$ is equal to the specific internal energy of the corresponding specie flux by neglecting the pressure work. The internal energy density is written in terms of the Helmholtz free energy density ψ and the specific entropy $\mathfrak{s}$ under the Legendre transformation as

$$\rho\mathfrak{e} = \psi + T\rho\mathfrak{s}\,. \tag{20}$$

Using Eqs. (18) and (20), the specific entropy $\mathfrak{s}$ in Eq. (19) can be substituted by the specific internal energy $\mathfrak{e}$ and the free energy density ψ. In addition, we define the chemical potentials of species as

$$\mu_{\mathrm{M}} = \mathfrak{e}^{\mathrm{f}}_{\mathrm{M}} - T\mathfrak{s}^{\mathrm{f}}_{\mathrm{M}} \quad \mu_{\mathrm{H}} = \mathfrak{e}^{\mathrm{f}}_{\mathrm{H}} - T\mathfrak{s}^{\mathrm{f}}_{\mathrm{H}}\,. \tag{21}$$

As a result, the dissipation inequality leads to the global dissipation postulation for isothermal processes with $r = 0$, $\nabla\cdot\boldsymbol{q} = 0$ and $\nabla T = 0$

$$D = \int_{\Omega}\boldsymbol{b}_{\mathrm{f}}\cdot\dot{\boldsymbol{u}}\,dV + \int_{\partial\Omega}\left(\boldsymbol{t}_{\mathrm{f}}\cdot\dot{\boldsymbol{u}} + t_{\mathrm{M}}\dot{c}_{\mathrm{M}} + t_{\mathrm{H}}\dot{c}_{\mathrm{H}} - \mu_{\mathrm{M}}\boldsymbol{h}_{\mathrm{M}}\cdot\boldsymbol{n} - \mu_{\mathrm{H}}\boldsymbol{h}_{\mathrm{H}}\cdot\boldsymbol{n}\right)\,dA - \int_{\Omega}\dot{\psi}\,dV \geq 0\,. \tag{22}$$

By applying divergence theorem, we then obtain

$$\begin{aligned}D = \int_{\Omega}\big(&\boldsymbol{b}_{\mathrm{f}}\cdot\dot{\boldsymbol{u}} + \mathrm{div}\boldsymbol{\sigma}\cdot\dot{\boldsymbol{u}} + \boldsymbol{\sigma} : \dot{\boldsymbol{\varepsilon}} + \nabla\cdot\boldsymbol{\xi}_{\mathrm{M}}\dot{c}_{\mathrm{M}} + \boldsymbol{\xi}_{\mathrm{M}}\cdot\nabla\dot{c}_{\mathrm{M}} + \nabla\cdot\boldsymbol{\xi}_{\mathrm{H}}\dot{c}_{\mathrm{H}} + \boldsymbol{\xi}_{\mathrm{H}}\cdot\nabla\dot{c}_{\mathrm{H}} - \mu_{\mathrm{M}}\nabla\cdot\boldsymbol{h}_{\mathrm{M}} \\ &-\nabla\mu_{\mathrm{M}}\cdot\boldsymbol{h}_{\mathrm{M}} - \mu_{\mathrm{H}}\nabla\cdot\boldsymbol{h}_{\mathrm{H}} - \nabla\mu_{\mathrm{H}}\cdot\boldsymbol{h}_{\mathrm{H}} - \dot{\psi}\big)\,dV \geq 0\,,\end{aligned} \tag{23}$$

which must be hold for all parts of the domain Ω. Using the mass balance of species in Eqs. (4) and (5) and force balance equations in Eqs. (12)–(14), the local dissipation inequality can be expressed as

$$\mathcal{D} = \boldsymbol{\sigma} : \dot{\boldsymbol{\varepsilon}} + \tilde{\mu}_{\mathrm{M}}\dot{c}_{\mathrm{M}} + \boldsymbol{\xi}_{\mathrm{M}}\cdot\nabla\dot{c}_{\mathrm{M}} + \tilde{\mu}_{\mathrm{H}}\dot{c}_{\mathrm{H}} + \boldsymbol{\xi}_{\mathrm{H}}\cdot\nabla\dot{c}_{\mathrm{H}} - \nabla\mu_{\mathrm{M}}\cdot\boldsymbol{h}_{\mathrm{M}} - \nabla\mu_{\mathrm{H}}\cdot\boldsymbol{h}_{\mathrm{H}} - \dot{\psi} \geq 0 \tag{24}$$

where the net chemical potentials $\tilde{\mu}_{\mathrm{M}}$ and $\tilde{\mu}_{\mathrm{H}}$ are defined as

$$\tilde{\mu}_{\mathrm{M}} := \omega_{\mathrm{M}} + \mu_{\mathrm{M}}\,, \quad \tilde{\mu}_{\mathrm{H}} := \omega_{\mathrm{H}} + \mu_{\mathrm{H}}\,. \tag{25}$$

2.6. Specification of free energy density function

The free energy density is decomposed into the elasto-plastic part and the electrochemical part as

$$\psi = \psi^{\mathrm{ep}} + \psi^{\mathrm{ch}} = \psi^{\mathrm{ep}}(\boldsymbol{\varepsilon}, \boldsymbol{\varepsilon}^{\mathrm{p}}, \gamma, \phi_{\mathrm{d}}) + \psi^{\mathrm{ch}}(\phi_{\mathrm{c}}, c_{\mathrm{M}}, \nabla c_{\mathrm{M}}, c_{\mathrm{H}}, \nabla c_{\mathrm{H}})\,. \tag{26}$$

The elasto-plastic free energy density ψ^{ep} depends on the total strain $\boldsymbol{\varepsilon}$, the plastic strain $\boldsymbol{\varepsilon}^{\mathrm{p}}$, the equivalent plastic strain γ and the fracture phase-field ϕ_{d}. To prevent the interpenetration of the crack region under compression, the volumetric/deviatoric split method proposed by Amor et al. [44] is utilised in the formulation of the elastic free energy density. In this context, the strain tensor is decomposed into its spherical and deviatoric parts

$$\boldsymbol{\varepsilon} = \boldsymbol{\varepsilon}_{\mathrm{S}} + \boldsymbol{\varepsilon}_{\mathrm{D}}\,, \quad \boldsymbol{\varepsilon}_{\mathrm{S}} = \frac{1}{3}\mathrm{tr}(\boldsymbol{\varepsilon})\boldsymbol{I}, \quad \boldsymbol{\varepsilon}_{\mathrm{D}} = \boldsymbol{\varepsilon} - \frac{1}{3}\mathrm{tr}(\boldsymbol{\varepsilon})\boldsymbol{I}\,, \tag{27}$$

where $\boldsymbol{I}$ is the second-order identity tensor. By introducing the elastic deviatoric strain $\boldsymbol{\varepsilon}_{\mathrm{D}}^{\mathrm{e}} = \boldsymbol{\varepsilon}_{\mathrm{D}} - \boldsymbol{\varepsilon}_{\mathrm{D}}^{\mathrm{p}}$, where $\boldsymbol{\varepsilon}_{\mathrm{D}}^{\mathrm{p}} := \boldsymbol{\varepsilon}^{\mathrm{p}} - \frac{1}{3}\mathrm{tr}(\boldsymbol{\varepsilon}^{\mathrm{p}})\boldsymbol{I}$ is the deviatoric part of the plastic strain tensor, the elastic–plastic free energy density is defined as a combination of the elastic free energy density ψ^{el} and the free energy density ψ^{hard} due to the isotropic hardening as:

$$\psi^{\mathrm{ep}} = \psi^{\mathrm{el}}(\boldsymbol{\varepsilon}, \boldsymbol{\varepsilon}^{\mathrm{p}}, \phi_{\mathrm{d}}, c_{\mathrm{H}}) + \psi^{\mathrm{hard}}(\gamma, \phi_{\mathrm{d}}), \tag{28}$$

with

$$\begin{aligned}\psi^{\mathrm{el}}(\boldsymbol{\varepsilon}, \boldsymbol{\varepsilon}^{\mathrm{p}}, \phi_{\mathrm{d}}, c_{\mathrm{H}}) =& h_{\mathrm{d}}(\phi_{\mathrm{d}}) \left[\frac{1}{2}\bar{K}\langle \mathrm{tr}(\boldsymbol{\varepsilon} - \boldsymbol{\varepsilon}^{\mathrm{p}})\rangle^2 + \bar{G}\left(\boldsymbol{\varepsilon}_{\mathrm{D}} - \boldsymbol{\varepsilon}_{\mathrm{D}}^{\mathrm{p}}\right) : \left(\boldsymbol{\varepsilon}_{\mathrm{D}} - \boldsymbol{\varepsilon}_{\mathrm{D}}^{\mathrm{p}}\right)\right] + \frac{1}{2}\bar{K}\langle -\mathrm{tr}(\boldsymbol{\varepsilon} - \boldsymbol{\varepsilon}^{\mathrm{p}})\rangle^2 \\ & - h_{\mathrm{d}}(\phi_{\mathrm{d}})\bar{K}\bar{V}_{\mathrm{H}}\left(c_{\mathrm{H}} - c_{\mathrm{H0}}\right)\langle \mathrm{tr}(\boldsymbol{\varepsilon} - \boldsymbol{\varepsilon}^{\mathrm{p}})\rangle + \bar{K}\bar{V}_{\mathrm{H}}\left(c_{\mathrm{H}} - c_{\mathrm{H0}}\right)\langle -\mathrm{tr}(\boldsymbol{\varepsilon} - \boldsymbol{\varepsilon}^{\mathrm{p}})\rangle\end{aligned} \tag{29}$$

$$\psi^{\mathrm{hard}}(\gamma, \phi_{\mathrm{d}}) = \frac{1}{2}h_{\mathrm{d}}(\phi_{\mathrm{d}})\bar{H}\gamma^2. \tag{30}$$

In the elastic free energy density, we account for the volume expansion induced by hydrogen atoms. $\bar{K} > 0$ and $\bar{G} > 0$ are effective (undamaged) bulk and shear modulus respectively. $\bar{V}_{\mathrm{H}}$ is the partial molar volume of hydrogen in solid solution. c_{H0} is the reference hydrogen concentration. The degradation function, $h_{\mathrm{d}}(\phi_{\mathrm{d}}) = (1 - \phi_{\mathrm{d}})^2$, captures the degradation of the mechanical properties of material due to damage. For simplification, we ignore the effect of corrosion on mechanical deformations, since the deformation behaviour of corrosion products of biodegradable magnesium alloys are not available in literature. The Macauley brackets $\langle\cdot\rangle$ are defined as $\langle x\rangle = \max(x, 0)$. $\bar{H}$ is the effective hardening modulus. Eq. (29) implies that only the strain energy induced by tension and shear drives the damage and crack propagation in the material.

The chemical free energy density ψ^{ch} incorporates the bulk parts, $\psi^{\mathrm{M}}_{\mathrm{bulk}}$ and $\psi^{\mathrm{H}}_{\mathrm{bulk}}$, and the interfacial part $\psi^{\mathrm{ch}}_{\mathrm{grad}}$, which can be expressed as a function of the corrosion field ϕ_{c}, the Mg-ion concentration c_{M}, and hydrogen concentration c_{H}

$$\psi^{\mathrm{ch}}(c_{\mathrm{M}}, c_{\mathrm{H}}, \phi_{\mathrm{c}}, \nabla c_{\mathrm{M}}, \nabla c_{\mathrm{H}}) = \psi^{\mathrm{M}}_{\mathrm{bulk}}(c_{\mathrm{M}}, \phi_{\mathrm{c}}) + \psi^{\mathrm{H}}_{\mathrm{bulk}}(c_{\mathrm{H}}) + \psi^{\mathrm{ch}}_{\mathrm{grad}}(\nabla c_{\mathrm{M}}, \nabla c_{\mathrm{H}}), \tag{31}$$

where the interfacial energy density is given

$$\psi^{\mathrm{ch}}_{\mathrm{grad}} = \kappa_{\mathrm{M}}\nabla c_{\mathrm{M}} \cdot \nabla c_{\mathrm{M}} + \kappa_{\mathrm{H}}\nabla c_{\mathrm{H}} \cdot \nabla c_{\mathrm{H}}. \tag{32}$$

Here, κ_{M} and κ_{H} are the concentration gradient energy coefficients for Mg and H concentration, respectively [45]. The magnesium chemical bulk free energy is constructed following the KKS model [46] as [47]

$$\psi^{\mathrm{M}}_{\mathrm{bulk}}(c_{\mathrm{M}}, \phi_{\mathrm{c}}) = A\left[c^*_{\mathrm{M}} - \left(1 - h_{\mathrm{c}}(\phi_{\mathrm{c}})\right)c^*_{\mathrm{Le}} - h_{\mathrm{c}}(\phi_{\mathrm{c}})\right]^2. \tag{33}$$

Here, we define $c^*_{\mathrm{M}}(\boldsymbol{x}, t) = c_{\mathrm{M}}(\boldsymbol{x}, t)/c_{\mathrm{solid}}$ as the normalised Mg concentration field with c_{solid} being the equilibrium concentration of Mg in the solid. A is the free energy density curvature and c^*_{Le} is the normalised equilibrium Mg concentration in the corroded material. $h_{\mathrm{c}}(\phi_{\mathrm{c}})$ is a continuous interpolation function such that $h_{\mathrm{c}}(\phi_{\mathrm{c}} = 0) = 0$ and $h_{\mathrm{c}}(\phi_{\mathrm{c}} = 1) = 1$. In this study, a cubic function $h_{\mathrm{c}}(\phi_{\mathrm{c}}) = -2{\phi_{\mathrm{c}}}^3 + 3{\phi_{\mathrm{c}}}^2$ is used following [47]. To approximate the hydrogen bulk energy in a simple continuous manner, we consider it within a regular solution model following [48]

$$\psi^{\mathrm{H}}_{\mathrm{bulk}}(c_{\mathrm{H}}) = \mu_{\mathrm{H0}}c_{\mathrm{H}} + RTN\left[\eta\ln\eta + (1 - \eta)\ln(1 - \eta)\right]. \tag{34}$$

μ_{H0} is the reference hydrogen chemical potential and R is the gas constant. N is the density of lattice site and η represents the occupancy of the lattice sites. We denote the occupancy fraction of the lattice site by $\eta = c_{\mathrm{H}}/N$ with $0 \le \eta \le 1$. For the hcp lattice structure of magnesium alloys, the conditions of low occupancy $\eta \ll 1$ leads to

$$\psi^{\mathrm{H}}_{\mathrm{bulk}}(c_{\mathrm{H}}) = \mu_{\mathrm{H0}}c_{\mathrm{H}} + RTc_{\mathrm{H}}\ln\frac{c_{\mathrm{H}}}{N}. \tag{35}$$

2.7. Constitutive relations

With the free energy density ψ being defined, the constitutive relations can be derived by fulfilling the free energy imbalance:

$$\begin{aligned}\mathcal{D} = &\left(\boldsymbol{\sigma} - \partial_{\boldsymbol{\varepsilon}}\psi\right) : \dot{\boldsymbol{\varepsilon}} + \left(\tilde{\mu}_{\mathrm{M}} - \partial_{c_{\mathrm{M}}}\psi\right)\dot{c}_{\mathrm{M}} + \left(\boldsymbol{\xi}_{\mathrm{d}} - \partial_{\nabla c_{\mathrm{M}}}\psi\right)\cdot\nabla\dot{c}_{\mathrm{M}} + \left(\tilde{\mu}_{\mathrm{H}} - \partial_{c_{\mathrm{H}}}\psi\right)\dot{c}_{\mathrm{H}} \\ &+ \left(\boldsymbol{\xi}_{\mathrm{H}} - \partial_{\nabla c_{\mathrm{H}}}\psi\right)\cdot\nabla\dot{c}_{\mathrm{H}} - \partial_{\phi_{\mathrm{d}}}\psi\dot{\phi}_{\mathrm{d}} - \partial_{\varepsilon^{\mathrm{p}}}\psi\dot{\varepsilon}^{\mathrm{p}} - \partial_{\gamma}\psi\dot{\gamma} - \partial_{\phi_{\mathrm{c}}}\psi\dot{\phi}_{\mathrm{c}} - \nabla\mu_{\mathrm{M}}\cdot\boldsymbol{h}_{\mathrm{M}} - \nabla\mu_{\mathrm{H}}\cdot\boldsymbol{h}_{\mathrm{H}} \ge 0.\end{aligned} \tag{36}$$

To fulfil the dissipation inequality condition for all admissible thermodynamic processes, we determine the stress $\boldsymbol{\sigma}$, the net Mg-chemical potential $\tilde{\mu}_{\mathrm{M}}$, the Mg-microstress $\boldsymbol{\xi}_{\mathrm{M}}$, the net H-chemical potential $\tilde{\mu}_{\mathrm{H}}$, and the H-microstress $\boldsymbol{\xi}_{\mathrm{H}}$ as

$$\boldsymbol{\sigma} = \partial_{\boldsymbol{\varepsilon}}\psi, \quad \tilde{\mu}_{\mathrm{M}} = \partial_{c_{\mathrm{M}}}\psi, \quad \boldsymbol{\xi}_{\mathrm{M}} = \partial_{\nabla c_{\mathrm{M}}}\psi, \quad \tilde{\mu}_{\mathrm{H}} = \partial_{c_{\mathrm{H}}}\psi, \quad \boldsymbol{\xi}_{\mathrm{H}} = \partial_{\nabla c_{\mathrm{H}}}\psi. \tag{37}$$

Then, by defining $\boldsymbol{s}_{\mathrm{p}} = -\partial_{\varepsilon^{\mathrm{p}}}\psi = \boldsymbol{\sigma}$, $s_{\gamma} = -\partial_{\gamma}\psi = h_{\mathrm{d}}\bar{H}$, $s_{\phi_{\mathrm{d}}} = -\partial_{\phi_{\mathrm{d}}}\psi$, $s_{\phi_{\mathrm{c}}} = -\partial_{\phi_{\mathrm{c}}}\psi$, $\boldsymbol{s}_{\mathrm{M}} = -\nabla\mu_{\mathrm{M}}$ and $\boldsymbol{s}_{\mathrm{H}} = -\nabla\mu_{\mathrm{H}}$ as dissipative forces, the reduced local dissipation inequality renders

$$\mathcal{D} = \boldsymbol{\sigma}\dot{\varepsilon}^{\mathrm{p}} + s_{\gamma}\dot{\gamma} + s_{\phi_{\mathrm{d}}}\dot{\phi}_{\mathrm{d}} + s_{\phi_{\mathrm{c}}}\dot{\phi}_{\mathrm{c}} + \boldsymbol{s}_{\mathrm{M}}\cdot\boldsymbol{h}_{\mathrm{M}} + \boldsymbol{s}_{\mathrm{H}}\cdot\boldsymbol{h}_{\mathrm{H}} \ge 0 \tag{38}$$

Therefore, the dissipation during degradation and fracture processes in biodegradable magnesium alloys is attributed to plastic deformation, fracture, electrochemical reaction and diffusion. Furthermore, the mentioned dissipation processes should satisfy the dissipation inequality individually.

2.7.1. Evolution of plastic deformations

The derivation of the evolution equations for $\dot{\varepsilon}^{\mathrm{p}}$ and $\dot{\gamma}$ is based on the principle of maximum dissipation. Together with the yield function f_{p}, we introduce the Lagrangean functional

$$\mathcal{L}_{\mathrm{p}} = \boldsymbol{\sigma}\dot{\varepsilon}^{\mathrm{p}} + s_{\gamma}\dot{\gamma} - \lambda_{\mathrm{p}} f_{\mathrm{p}}\,, \quad \text{subject to} \quad \lambda_{\mathrm{p}} \geq 0\,,\ f_{\mathrm{p}} \leq 0 \,\text{and}\, \lambda_{\mathrm{p}} f_{\mathrm{p}} = 0\,, \tag{39}$$

where λ_{p} is the plastic Lagrange multiplier, which enforces the restriction on yield surface. By assuming isotropic plastic deformations of magnesium alloys, the yield function is defined according to the J_2 plasticity theory as

$$f_{\mathrm{p}}(\boldsymbol{\sigma}, s_{\gamma}; \boldsymbol{\varepsilon}^{\mathrm{p}}, \gamma, \phi_{\mathrm{d}}) := \sqrt{\frac{3}{2}}\|\mathrm{dev}[\boldsymbol{\sigma}]\| + s_{\gamma} - \sigma_{\mathrm{y}} \leq 0, \tag{40}$$

where $\mathrm{dev}[\boldsymbol{\sigma}]$ is the deviatoric part of the stress tensor. σ_{y} is the degraded initial yield stress of materials with the corrosion state ϕ_{d}, which is computed with the degradation function $h_{\mathrm{d}}(\phi_{\mathrm{d}})$ and the initial yield stress of uncorroded materials $\bar{\sigma}_{\mathrm{y}}$

$$\sigma_{\mathrm{y}} = h_{\mathrm{d}}(\phi_{\mathrm{d}})\bar{\sigma}_{\mathrm{y}}\,. \tag{41}$$

The evolution equations for ε^{p} and γ can obtained by taking derivatives with respect to $\boldsymbol{\sigma}$ and σ_{γ} as

$$\frac{\partial \mathcal{L}_{\mathrm{p}}}{\partial \boldsymbol{\sigma}} = \dot{\varepsilon}^{\mathrm{p}} - \lambda_{\mathrm{p}}\sqrt{\frac{3}{2}}\frac{\mathrm{dev}[\boldsymbol{\sigma}]}{\|\mathrm{dev}[\boldsymbol{\sigma}]\|} = 0 \tag{42}$$

$$\frac{\partial \mathcal{L}_{\mathrm{p}}}{\partial s_{\gamma}} = \dot{\gamma} - \lambda_{\mathrm{p}} = 0\,, \tag{43}$$

which can be further rewritten as

$$\dot{\varepsilon}^{\mathrm{p}} - \dot{\gamma}\sqrt{\frac{3}{2}}\frac{\mathrm{dev}[\boldsymbol{\sigma}]}{\|\mathrm{dev}[\boldsymbol{\sigma}]\|} = 0\,. \tag{44}$$

Due to γ being a scalar, Eq. (44) shows that the plastic strain rate $\dot{\varepsilon}^{\mathrm{p}}$ and the deviatoric stress $\mathrm{dev}[\boldsymbol{\sigma}]$ are coaxial. Thus, one obtains the relations

$$\frac{\dot{\boldsymbol{\varepsilon}}^{\mathrm{p}}}{\|\dot{\boldsymbol{\varepsilon}}^{\mathrm{p}}\|} = \frac{\mathrm{dev}[\boldsymbol{\sigma}]}{\|\mathrm{dev}[\boldsymbol{\sigma}]\|} \quad \text{and} \quad \dot{\gamma} = \sqrt{\frac{2}{3}}\|\dot{\boldsymbol{\varepsilon}}^{\mathrm{p}}\|\,. \tag{45}$$

The plastic dissipation

$$\mathcal{D}_{\mathrm{p}} = \boldsymbol{\sigma}\dot{\varepsilon}^{\mathrm{p}} + s_{\gamma}\dot{\gamma} = \sigma_{y}\dot{\gamma} \geq 0 \tag{46}$$

always holds for $\sigma_{y} \geq 0$ and $\dot{\gamma} \geq 0$.

2.7.2. Evolution of the regularised crack surface

With the assumption of plastic incompressibility, the trace of plastic strain $tr(\boldsymbol{\varepsilon}^{\mathrm{p}})$ is equal to 0 and its deviatoric component is identical to itself $\dot{\boldsymbol{\varepsilon}}^{\mathrm{p}}_{D} = \dot{\boldsymbol{\varepsilon}}^{\mathrm{p}}$. The Lagrangean functional for the dissipative process of fracture is expressed as

$$\mathcal{L}_{\mathrm{d}} = s_{\phi_{\mathrm{d}}}\dot{\phi}_{\mathrm{d}} - \lambda_{\mathrm{d}} f_{\mathrm{d}}\,, \quad \text{subject to} \quad \lambda_{\mathrm{d}} \geq 0\,,\ f_{\mathrm{d}} \leq 0 \,\text{and}\, \lambda_{\mathrm{d}} f_{\mathrm{d}} = 0\,, \tag{47}$$

where λ_{d} is the fracture Lagrange multiplier. Regarding the rate-independent crack evolution process with a threshold condition, the local fracture threshold function f_{d} is introduced as

$$f_{\mathrm{d}}(s_{\phi_{\mathrm{d}}}; \gamma, \phi_{\mathrm{d}}) = s_{\phi_{\mathrm{d}}} + \zeta_{\mathrm{pd}} - r_{\mathrm{d}} \quad \text{with} \quad r_{\mathrm{d}} := g_{\mathrm{d}}\delta_{\phi_{\mathrm{d}}}\chi(\phi_{\mathrm{d}}, \nabla\phi_{\mathrm{d}})\,. \tag{48}$$

$\zeta_{\mathrm{pd}} = -h'_{\mathrm{d}}\bar{\sigma}_{\mathrm{y}}\gamma$ is an additional coupling force introduced by in [49,50] to render a strong interplay between plastic and fracture dissipative processes. r_{d} is the fracture resistance of the regularised crack surface depending on the intrinsic fracture toughness of material and the smeared crack surface topology, which are characterised by the critical fracture energy g_{d} and the fracture surface density function χ, respectively. $\delta_{\phi_{\mathrm{d}}}\chi(\phi_{\mathrm{d}}, \nabla\phi_{\mathrm{d}})$ is the variational derivative of $\chi(\phi_{\mathrm{d}}, \nabla\phi_{\mathrm{d}})$ and defined as

$$\delta_{\phi_{\mathrm{d}}}\chi(\phi_{\mathrm{d}}, \nabla\phi_{\mathrm{d}}) := \partial_{\phi_{\mathrm{d}}}\chi - \nabla\cdot\partial_{\nabla\phi_{\mathrm{d}}}\chi\,, \quad \text{with} \quad \chi(\phi_{\mathrm{d}}, \nabla\phi_{\mathrm{d}}) = \frac{l_{\mathrm{d}}}{2}\nabla\phi_{\mathrm{d}}\cdot\nabla\phi_{\mathrm{d}} + \frac{{\phi_{\mathrm{d}}}^2}{2l_{\mathrm{d}}}\,, \tag{49}$$

where l_{d} is the length scale parameter adopted in the phase-field framework to regularise the sharp crack surface topology to a diffusive crack surface. By taking the derivative with respect to $s_{\phi_{\mathrm{d}}}$, we obtain the evolution law for ϕ_{d} with

$$\frac{\partial \mathcal{L}_{\mathrm{d}}}{\partial s_{\phi_{\mathrm{d}}}} = \dot{\phi}_{\mathrm{d}} - \lambda_{\mathrm{d}} = 0\,. \tag{50}$$

The constraint $\dot{\phi}_{\mathrm{d}} \geq 0$ for the crack field is used to fulfil the irreversibility of damage.

In the proposed model, g_{d} is the fracture energy required to form a unit area of crack and considered to decrease during the corrosion and hydrogen embrittlement processes as a function of the corrosion field ϕ_{d} and the hydrogen concentration c_{H}, that is

$$g_{\mathrm{d}}(\phi_{\mathrm{c}}, c_{\mathrm{H}}) = h_{\mathrm{dc}}(\phi_{\mathrm{c}})h_{\mathrm{dh}}(c_{\mathrm{H}})g_{\mathrm{dm}} + [1 - h_{\mathrm{dc}}(\phi_{\mathrm{c}})]g_{\mathrm{dc}}\,, \tag{51}$$

where g_{dm} and g_{dc} are the fracture energy of uncorroded material and totally corroded material, respectively. h_{dh} captures the weakening of fracture toughness of the uncorroded material by hydrogen

$$h_{dh}(c_H) = 1 - \Lambda^{\theta} \quad \text{with} \quad \theta = \frac{c_H}{c_H + \exp(\frac{-\Delta G_b^0}{RT})}, \tag{52}$$

where Λ is the damage coefficient that weights the hydrogen-lowering of the critical fracture energy [51]. ΔG_b^0 is the Gibbs free energy difference between the decohering interface and surrounding material. The degradation function h_{dc} depending on corrosion is constructed as

$$h_{dc}(\phi_c) = -m_c \phi_c^{m_c+1} + (m_c + 1)\phi_c^{m_c}, \tag{53}$$

where $m_d \geq 2$ is a model parameter [31]. The cubic function ($m_d = 2$) is introduced by Kuhn et al. [52] and the quartic function ($m_d = 3$) is adopted by Karma et al. in [53]. Moreover, Dittmann et al. [54] proposed that the critical fracture energy is decreased by the total plastic work. Accordingly, we assume the degradation function for the critical energy of the uncorroded and totally corroded materials g_{dm} and g_{dc} depending on the accumulated plastic strain γ as

$$g_{dm} := g_{dm\infty} + (g_{dm0} - g_{dm\infty})\exp(-(\gamma/\gamma_{crit})^{m_p}), \tag{54}$$

where γ_{crit} is the critical value of the accumulated plastic strain for effects of plastic deformations, and m_p is the model parameter associated with the accumulated plastic strain γ. Therein, subscripts 0 and ∞ indicate the values of critical energy taken at the initial and saturated stages, respectively.

The fracture threshold function and inequality constrain give the fracture KKT conditions

$$\dot{\phi}_d \geq 0, \; f_d \leq 0 \text{ and } \dot{\phi}_d f_d = 0. \tag{55}$$

Considering the loading and unloading processes for Eq. (48), the fracture KKT conditions result in

$$s_{\phi_d} - h_d' \bar{\sigma}_y \gamma \begin{cases} = r_d & \text{for } \dot{\phi}_d > 0 \\ < r_d & \text{for } \dot{\phi}_d = 0 \end{cases}. \tag{56}$$

By denoting $\bar{\psi}^{ep+} := \frac{1}{2}\bar{K}\langle \mathrm{tr}(\boldsymbol{\varepsilon} - \boldsymbol{\varepsilon}^p)\rangle^2 + \bar{G}(\boldsymbol{\varepsilon} - \boldsymbol{\varepsilon}^p) : (\boldsymbol{\varepsilon} - \boldsymbol{\varepsilon}^p) - \bar{K}\bar{V}_H\left(c_H - c_{H0}\right)\langle \mathrm{tr}(\boldsymbol{\varepsilon} - \boldsymbol{\varepsilon}^p)\rangle + \frac{1}{2}\bar{H}\gamma^2$ as the effective positive elasto-plastic free energy and recalling $s_{\phi_d} = -\partial_{\phi_d}\psi = -h_d'\bar{\psi}^{ep+}$, we have

$$-h_d'\left(\bar{\psi}^{ep+} + \bar{\sigma}_y\gamma\right) \begin{cases} = r_d & \text{for } \dot{\phi}_d > 0 \\ < r_d & \text{for } \dot{\phi}_d = 0 \end{cases}, \tag{57}$$

To ensure the irreversibility condition for the crack evolution equations, a local history maximum driving energy is introduced following Borden et al. [55]

$$\mathcal{H} := \max_{\tau \in [0,t]} \left(\bar{\psi}^{ep+} + \bar{\sigma}_y\gamma\right). \tag{58}$$

Substituting $\bar{\psi}^{ep+} + \bar{\sigma}_y\gamma$ with $\mathcal{H}$, the evolution Eq. (57) for the crack phase-field variable can be rewritten as

$$-h_d'\mathcal{H} + \frac{g_d}{l_d}(l_d^2\nabla\cdot\nabla\phi_d - \phi_d) = 0. \tag{59}$$

The fracture dissipation

$$D_d = -h_d'\bar{\psi}^{ep+}\dot{\phi}_d \geq 0 \tag{60}$$

always holds for $-h_d'\bar{\psi}^{ep+} \geq 0$ and $\dot{\phi}_d \geq 0$.

2.7.3. Evolution of corrosion interface and species transport

In order to define the evolution law related to the corrosion dissipative process, the existence of a reaction–diffusion dissipation potential function $v(s_{\phi_c}, \boldsymbol{s}_M, \boldsymbol{s}_H)$ is assumed. The specific form is given

$$v(s_{\phi_c}, \boldsymbol{s}_M, \boldsymbol{s}_H) = \frac{L_{\phi_c}}{2}\langle r_c - \zeta_{dc} - s_{\phi_c}\rangle^2 + \frac{M_M}{2}\boldsymbol{s}_M\cdot\boldsymbol{s}_M + \frac{M_H}{2}\boldsymbol{s}_H\cdot\boldsymbol{s}_H \tag{61}$$

Here, L_{ϕ_c} is the interface kinetics parameter of corrosion. The Macaulay bracket is used to enforce the corrosion irreversibility $\dot{\phi}_c \leq 0$ considering ϕ_c decreasing from 1 to 0. $\zeta_{dc} := -\partial_{\phi_c} g_d \chi$ is an additional coupling force introduced in [31] considering that fracture triggers additional microgalvanic cell reaction between the fresh-exposed damaged area and the barrier film. M_M and M_H are the diffusion mobility of Mg specie and hydrogen transport, respectively. They are related with their diffusion coefficient as $M_M = \frac{D_M}{2A}c_{solid}^2$ and $M_H = \frac{D_H c_H}{RT}$. Specially, we adopt the assumption that diffusion coefficients are functions of the crack phase-field variable ϕ_d. A crack filled with electrolyte creates a path for a rapid diffusion of materials, and therefore, it is expected that the diffusion coefficient within a crack is much higher than that in intact regions. To this end, a linear function is employed to interpolate the change of the diffusion coefficient D_* with $*\in\{M, H\}$ between cracked and intact regions following Wu et al. [56]

$$D_*(\phi_c) = (1 - h_f(\phi_d))D_{*p} + h_f(\phi_d)D_{*l}, \quad \text{and} \quad h_f(\phi_d) = \phi_d^{m_d}, \tag{62}$$

where m_{d} denotes a model parameter controlling the rate of diffusivity change. $D_{*\mathrm{p}}$ and $D_{*\mathrm{l}}$ are the diffusion coefficient of species in the intact material and the electrolyte, respectively. r_{c} is the corrosion threshold and defined by

$$r_{\mathrm{c}} := w_{\mathrm{c}}\partial_{\phi_{\mathrm{c}}} g_{\mathrm{w}}(\phi_{\mathrm{c}}) - \alpha_{\mathrm{c}}\,\nabla\cdot\nabla\phi_{\mathrm{c}}\,, \tag{63}$$

where α_{c} is the gradient energy coefficient associated with the corrosion field. $g_{\mathrm{w}}(\phi_{\mathrm{c}}) = {\phi_{\mathrm{c}}}^2(1-\phi_{\mathrm{c}})^2$ is the chemical double well potential, and w_{c} is the height of the imposed double-well energy barrier. The evolution laws for corrosion phase-field variable, Mg and H transport are derived from the dissipation potential as

$$\dot{\phi}_{\mathrm{c}} = \frac{\partial v}{\partial s_{\phi_{\mathrm{c}}}} = -L_{\phi_{\mathrm{c}}}\langle r_{\mathrm{c}} - \zeta_{\mathrm{dc}} - s_{\phi_{\mathrm{c}}}\rangle\,, \tag{64}$$

$$\boldsymbol{h}_{\mathrm{M}} = \frac{\partial v}{\partial \boldsymbol{s}_{\mathrm{M}}} = -M_{\mathrm{M}}\nabla\mu_{\mathrm{M}}\,, \tag{65}$$

$$\boldsymbol{h}_{\mathrm{H}} = \frac{\partial v}{\partial \boldsymbol{s}_{\mathrm{H}}} = -M_{\mathrm{H}}\nabla\mu_{\mathrm{H}}\,. \tag{66}$$

In the KKS model [46], c^*_{M} is the specie concentration for a mixture of the two phases with different chemical free energy density ψ_{S} and ψ_{L}

$$c^*_{\mathrm{M}} = h_{\mathrm{c}}(\phi_{\mathrm{c}})c^*_{\mathrm{S}} + \left[1 - h_{\mathrm{c}}(\phi_{\mathrm{c}})\right]c^*_{\mathrm{L}}\,, \tag{67}$$

where c^*_{S} and c^*_{L} are the normalised concentration of the coexisting metal phase and corrosion phase at a material point. The KKS model assumes that two phases of the mixture in dilute solutions has different concentrations but the identical chemical potential in a chemical equilibrium state

$$\frac{\partial\psi_{\mathrm{S}}}{\partial c^*_{\mathrm{S}}} = \frac{\partial\psi_{\mathrm{L}}}{\partial c^*_{\mathrm{L}}}\,,\quad \psi_{\mathrm{S}} = A(c^*_{\mathrm{S}}-1)^2\,,\quad \psi_{\mathrm{L}} = A(c^*_{\mathrm{L}} - c^*_{\mathrm{Le}})^2\,. \tag{68}$$

Combining these relations yields

$$c^*_{\mathrm{M}} = c^*_{\mathrm{S}} + (1 - h_{\mathrm{c}}(\phi_{\mathrm{c}}))(c^*_{\mathrm{Le}} - 1)\,. \tag{69}$$

The corrosion dissipative force is then

$$s_{\phi_{\mathrm{c}}} = -\partial_{\phi_{\mathrm{c}}}\psi = 2Ah'_{\mathrm{c}}(1-c^*_{Le})\left[c^*_{\mathrm{M}} - \left(1-h_{\mathrm{c}}(\phi_{\mathrm{c}})\right)c^*_{\mathrm{Le}} - h_{\mathrm{c}}(\phi_{\mathrm{c}})\right] = 2Ah'_{\mathrm{c}}(1-c^*_{Le})(c^*_{\mathrm{S}}-1) \le 0\,, \tag{70}$$

where the conditions $A > 0$, $h'_{\mathrm{c}} \ge 0$, $0 < c^*_{\mathrm{Le}} < 1$ and $0 < c^*_{\mathrm{S}} \le 1$ lead to $s_{\phi_{\mathrm{c}}} \le 0$. Therefore, the corrosion and diffusion dissipation

$$\mathcal{D}_{\mathrm{c}} = s_{\phi_{\mathrm{c}}}\dot{\phi}_{\mathrm{c}} + \boldsymbol{s}_{\mathrm{M}}\cdot\boldsymbol{h}_{\mathrm{M}} + \boldsymbol{s}_{\mathrm{H}}\cdot\boldsymbol{h}_{\mathrm{H}} = s_{\phi_{\mathrm{c}}}\dot{\phi}_{\mathrm{c}} + M_{\mathrm{M}}\nabla\mu_{\mathrm{M}}\cdot\nabla\mu_{\mathrm{M}} + M_{\mathrm{H}}\nabla\mu_{\mathrm{H}}\cdot\nabla\mu_{\mathrm{H}} \ge 0 \tag{71}$$

always holds for $s_{\phi_{\mathrm{c}}} \le 0$, $\dot{\phi}_{\mathrm{c}} \le 0$, $M_{\mathrm{M}} \ge 0$ and $M_{\mathrm{H}} \ge 0$.

2.8. Governing equations and boundary conditions

In this section, we collect the results to summarise the set of governing equations for the basic fields of the theory. This set of equations is obtained by combining the force balances and constitutive theory. The governing equations consist of:

① The stress balance equation

$$\nabla\cdot\boldsymbol{\sigma} + \boldsymbol{b}_{\mathrm{f}} = 0\,, \tag{72}$$

where $\boldsymbol{\sigma} = \partial_{\varepsilon}\psi = \mathbb{C} : (\varepsilon - \varepsilon^{\mathrm{p}}) - K\bar{V}_{\mathrm{H}}(c_{\mathrm{H}} - c_{\mathrm{H0}})\boldsymbol{I}$. $\mathbb{C}$ is the fourth-order symmetric elasticity tensor and given by

$$\mathbb{C}_{ijkl} = K\delta_{ij}\delta_{kl} + h_d\bar{G}(\delta_{ik}\delta_{jl} + \delta_{il}\delta_{jk} - \frac{2}{3}\delta_{ij}\delta_{kl})\,,\ \text{with}\ K = \begin{cases} h_d\bar{K} & \text{for } \mathrm{tr}(\boldsymbol{\varepsilon} - \boldsymbol{\varepsilon}^{\mathrm{p}}) \ge 0 \\ \bar{K} & \text{for } \mathrm{tr}(\boldsymbol{\varepsilon} - \boldsymbol{\varepsilon}^{\mathrm{p}}) < 0 \end{cases}. \tag{73}$$

$\boldsymbol{I}$ is the second order identity tensor. Considering the insubstantial effect of the second term in stress tensor on hydrogen embrittlement [57], it is neglected in the following simulations.

② The balance equation for fracture field

$$-h'_{\mathrm{d}}\mathcal{H} + \frac{g_{\mathrm{d}}}{l_{\mathrm{d}}}(l^2_{\mathrm{d}}\nabla\cdot\nabla\phi_{\mathrm{d}} - \phi_{\mathrm{d}}) = 0\,. \tag{74}$$

③ The evolution equation for the corrosion field

$$\dot{\phi}_{\mathrm{c}} = -L_{\phi_{\mathrm{c}}}\langle r_{\mathrm{c}} - \zeta_{\mathrm{dc}} - s_{\phi_{\mathrm{c}}}\rangle\,. \tag{75}$$

④ The balance equation for the species concentration

$$\dot{c}_{\mathrm{M}} = \nabla\cdot M_{\mathrm{M}}\nabla\mu_{\mathrm{M}}\,, \tag{76}$$

and

$$\dot{c}_{\mathrm{H}} = \nabla\cdot M_{\mathrm{H}}\nabla\mu_{\mathrm{H}}\,, \tag{77}$$

where by combining the definition of net chemical potential Eq. (25) and the equilibrium equations Eqs. (13), (14) and (37) the chemical potential μ_{M} and μ_{H} can be calculated as

$$\mu_{\mathrm{M}} = \partial_{c_{\mathrm{M}}}\psi - \nabla\cdot\partial_{\nabla c_{\mathrm{M}}}\psi\,, \tag{78}$$

and

$$\mu_{\mathrm{H}} = \partial_{c_{\mathrm{H}}}\psi - \nabla\cdot\partial_{\nabla c_{\mathrm{H}}}\psi\,. \tag{79}$$

It has been suggested that only one of the Laplacian terms ($\Delta\phi_{\mathrm{c}}$ or Δc) is sufficient to approximate the topology of corrosion interface [47], κ_{M} is assumed to be 0 for simplicity. Then, boundary condition $\bar{t}_{\mathrm{c}}\cdot\boldsymbol{n} = \kappa\nabla c_{\mathrm{M}} = 0$ holds on $\partial\Omega^{t}_{\mathrm{c}}$. Therefore, with the specification of chemical free energy function Eq. (31), the Mg chemical potential Eq. (78) becomes a local equation

$$\mu_{\mathrm{M}} = \frac{2A}{c_{\mathrm{solid}}}\left[\frac{c_{\mathrm{M}}}{c_{\mathrm{solid}}} + (c^{*}_{\mathrm{Le}} - 1)(3\phi_{\mathrm{c}}^{2} - 2\phi_{\mathrm{c}}^{3}) - c^{*}_{\mathrm{Le}}\right]. \tag{80}$$

The Mg diffusion equation Eq. (76) is then

$$\dot{c}_{\mathrm{M}} = \nabla\cdot D_{\mathrm{M}}c_{\mathrm{solid}}\nabla\left[\frac{c_{\mathrm{M}}}{c_{\mathrm{solid}}} + (c^{*}_{\mathrm{Le}} - 1)(3\phi_{\mathrm{c}}^{2} - 2\phi_{\mathrm{c}}^{3}) - c^{*}_{\mathrm{Le}}\right]. \tag{81}$$

After choosing the nominalised Mg concentration field $c^{*}_{\mathrm{M}}(\boldsymbol{x},t) = c_{\mathrm{M}}(\boldsymbol{x},t)/c_{\mathrm{solid}}$ as a global primary field, the Mg diffusion equation is rewritten into the normalised form

$$\dot{c}^{*}_{\mathrm{M}} = \nabla\cdot D_{\mathrm{M}}\nabla\left[c^{*}_{\mathrm{M}} + (c^{*}_{\mathrm{Le}} - 1)(3\phi_{\mathrm{c}}^{2} - 2\phi_{\mathrm{c}}^{3}) - c^{*}_{\mathrm{Le}}\right]. \tag{82}$$

Considering the constant lattice sites ($\nabla N = 0$) and reference chemical potential ($\nabla\mu_{\mathrm{H}} = 0$), and neglecting the gradient energy $\kappa_{\mathrm{H}} = 0$ [43], Eqs. (77) and (79) can be combined into the classic diffusion equation

$$\dot{c}_{\mathrm{H}} = \nabla\cdot\frac{D_{\mathrm{H}}c_{\mathrm{H}}}{RT}\nabla\left(RT\ln\frac{c_{\mathrm{H}}}{N} - K\bar{V}_{\mathrm{H}}\mathrm{tr}(\boldsymbol{\varepsilon}-\boldsymbol{\varepsilon}^{\mathrm{p}})\right) = \nabla\cdot\left(D_{\mathrm{H}}\nabla c_{\mathrm{H}} - \frac{D_{\mathrm{H}}c_{\mathrm{H}}}{RT}\nabla\bar{V}_{\mathrm{H}}\boldsymbol{\sigma}_{\mathrm{HS}}\right), \tag{83}$$

with $\boldsymbol{\sigma}_{\mathrm{HS}}$ being hydrostatic stress and calculated as

$$\boldsymbol{\sigma}_{\mathrm{HS}} = K\mathrm{tr}(\boldsymbol{\varepsilon}-\boldsymbol{\varepsilon}^{\mathrm{p}})\,. \tag{84}$$

Note that, the electrolyte solution comes into contact with the magnesium alloy matrix through the microdefects in PEO coatings. Initially, the microdefects are filled with corrosive medium, in which the diffusion coefficient of species is identical to that in the dilute solution. However, in the long-term corrosion process, the deposition of corrosion products within the microdefects gradually reduces the diffusion coefficient to a value characteristic of the corrosion products. This reduction of diffusivity of species in microdefects is mathematically approximated following [35]

$$D_{*} = D_{*\mathrm{p}} + (D_{*\mathrm{l}} - D_{*\mathrm{p}})e^{-bt}\,, \tag{85}$$

where b is a evolution coefficient and t is the immersion time with unit in day.

In summary, in the present multiphase-field model, two auxiliary phase-field variables ϕ_{d} and ϕ_{c} are introduced. ϕ_{d} tracks the crack interface in solids with $\phi_{\mathrm{d}} = 0$ for intact material points and $\phi_{\mathrm{d}} = 1$ for completely fractured state. Furthermore, ϕ_{d} is a passive state field without corresponding external loading as $\nabla\phi_{\mathrm{d}}\cdot\boldsymbol{n} = 0$ on $\partial\Omega$. By defining $\phi_{\mathrm{c}} = 0$ for the totally corroded material and $\phi_{\mathrm{c}} = 1$ for the uncorroded alloy matrix, ϕ_{c} varies continuously across the corrosion interface. Considering ϕ_{c} being always 0 in the electrolyte and no corresponding external tractions on the solid boundary, the boundary conditions for the corrosion field are $\phi_{\mathrm{c}} = 0$ on $\partial\Omega_{\mathrm{l}}$ and $\nabla\phi_{\mathrm{c}}\cdot\boldsymbol{n} = 0$ on $\partial\Omega_{\mathrm{s}}$. Due to the neglecting of concentration gradient energy, the boundary conditions for species concentration are defined as $\nabla c^{*}_{\mathrm{M}}\cdot\boldsymbol{n} = 0$ and $\nabla c_{\mathrm{H}}\cdot\boldsymbol{n} = 0$ on $\partial\Omega_{\mathrm{s}}$, and $c^{*}_{\mathrm{M}} = \bar{c}^{*}_{\mathrm{M}}$ and $c_{\mathrm{H}} = \bar{c}_{\mathrm{H}}$ on $\partial\Omega_{\mathrm{l}}$. Globally, the state of the domain is characterised by displacement $\boldsymbol{u}(\boldsymbol{x},t)$, normalised Mg concentration $c^{*}_{\mathrm{M}}(\boldsymbol{x},t)$, H concentration $c_{\mathrm{H}}(\boldsymbol{x},t)$, crack phase-field variable $\phi_{\mathrm{d}}(\boldsymbol{x},t)$ and corrosion phase-field variable $\phi_{\mathrm{c}}(\boldsymbol{x},t)$.

The multiphysics interactions in the proposed model are illustrated in Fig. 2 and summarised as follows: (1) Elastoplastic deformations drive the fracture process via the local history maximum driving energy $\mathcal{H}$ and influences hydrogen diffusion via the term $\nabla\bar{V}_{\mathrm{H}}\sigma_{\mathrm{HS}}$, respectively; (2) Fracture of materials leads to degradation of their mechanical properties (h_{d}); (3) Fracture creates a path for a rapid diffusion of materials and thereby facilitates the diffusion of chemical species, which is captured by the correction function (h_{f}) in the diffusion coefficient; (4) Corrosion and hydrogen reduce the fracture toughness of materials via the degradation functions (h_{dc} and h_{dh}); (5) Fracture process accelerates the chemical reaction at the corrosion interface via the term $\zeta_{\mathrm{dc}} = -g'_{\mathrm{d}}\chi$.

3. Computational simulations

In this section, four computational models are employed to (1) demonstrate the effect of hydrogen embrittlement on the SCC behaviour of biodegradable magnesium alloys, (2) compare the proposed model with film rupture-dissolution-repassivation model for predicting the SCC behaviour, (3) validate the proposed model for the PEO-coated magnesium alloy WE43MEO by comparing with the results of *in vitro* experiments under pure chemical and mechanochemical loadings, and (4) numerically investigate the SCC mechanism of magnesium alloys with post-sealed coatings at the microscale. In Section 3.1, a notched plate subjected to SSRT loadings is used as a numerical example to evaluate the impact of environmental hydrogen diffusion on the SCC behaviour.

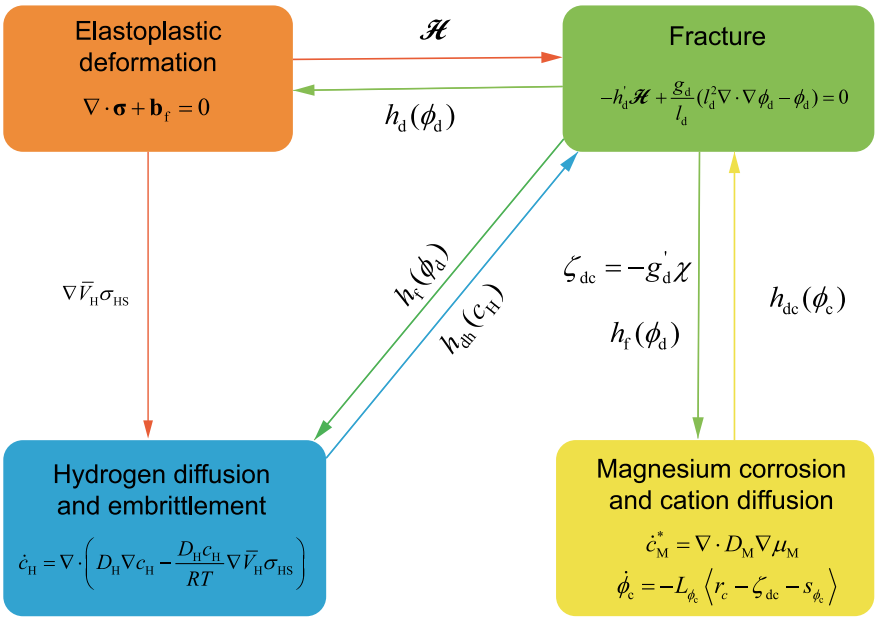

Fig. 2. Schematic of multiphysics interactions in the proposed model.

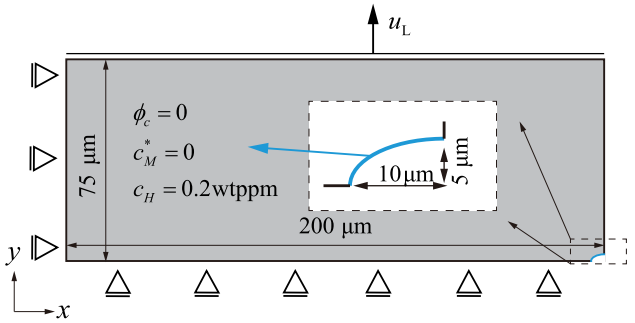

Fig. 3. Geometry and boundary conditions of the notched plate for studying the influences of hydrogen embrittlement.

Furthermore, by embedding a microscopic computational domain within a macroscopic specimen, we compare the simulation results of the present model with experimental observations in Section 3.3. Here, the corrosion rates of uncoated and coated specimens are analysed under purely corrosive conditions. In addition, we study the effect of static loadings on the damage evolution of coated magnesium alloy. In Section 3.4, a microscopic model of the magnesium alloy with a post-sealed PEO coating is used to study the SCC process under the SSRT conditions.

3.1. Notched plate: influences of hydrogen on the SCC behaviour of biodegradable magnesium alloys

In this numerical example, the proposed model is used to study the role of hydrogen embrittlement on the SCC process of the biodegradable magnesium rare-earth alloy WE43MEO (Meotec GmbH, Aachen). We consider a rectangular domain 200 μm × 150 μm containing an initial quarter-elliptic flaw on the right surface, subjected to stress corrosion. It has been known that inhomogeneous electrochemical properties between different phases of the material can result in barrier film breakdown, leading to the formation of microstructural flaws and the pit initiation. In this case, we demonstrate the influences of hydrogen on the pitting evolution process. The details of the computational example are depicted in Fig. 3. The model is discretised using fully integrated second-order 8-node plane strain elements with a mesh size of 0.5 μm. The material properties are listed in Table 1 based on the previous works [31,35]. The fracture interface thickness l_{d} is taken as 1/10 of the flaw width, while the critical fracture energy is adjusted with l_{d} to ensure that the material maintains the same tensile strength. The critical fracture energy of corrosion product g_{dc} is set to be $g_{\mathrm{dc}}=0.01g_{\mathrm{dm}}$.

In the computational simulations, $c^*=1$, $c_{\mathrm{H}}=0$ and $\phi_{\mathrm{c}}=1$ are defined as initial conditions in the notched bar, while $c^*=0$, $c_{\mathrm{H}}=0.2$ wtppm and $\phi_{\mathrm{c}}=0$ always hold at the notch as boundary conditions. Initially, the sample is precorroded for 1×10^5 s. Then, a displacement in the y-direction is applied along the upper edge with a constant slow loading rate 7.5×10^{-5} μm s^{-1}. On the other

Table 1
Model parameters of the magnesium alloy WE43MEO.

Parameter	Physical interpretation	Value
$\bar{H}$	Effective hardening modulus	770 MPa [31]
$\bar{K}$	Effective bulk modulus	32 173 MPa [31]
$\bar{G}$	Effective shear constant	17 480 MPa [31]
$\bar{\sigma}_y$	Effective initial yield stress	260 MPa [31]
l_{d}	Fracture interface thickness	0.001 mm
g_{dm0}	Initial critical fracture energy	0.85 MPa mm
$g_{\mathrm{dm}\infty}$	Reduced critical fracture energy	$0.15g_{dm0}$ [31]
m_{p}	Plastic model parameter	5 [31]
γ_{crit}	Critical equivalent plastic strain	0.8 [31]
c_{solid}	Saturated Mg-ion concentration	67.319 mol L^{-1} [31]
c^*_{Le}	Normalised saturated Mg-ion concentration in the corroded material	0.051 [31]
α_{c}	Gradient energy coefficient	5.1×10^{-5} N [35]
w_{c}	Height of the double-well energy barrier	3.528×10^{-2} J mm^{-3} [35]
A	Free energy density curvature	53.5 N mm^{-2} [35]
D_{Mp}	Diffusion coefficient of Mg in corrosion product	1.17×10^{-8} mm^2 s^{-1} [35]
D_{Ml}	Diffusion coefficient of Mg cations in electrolyte	8.5×10^{-4} mm^2 s^{-1} [31]
D_{Hp}	Diffusion coefficient of H in alloy	2×10^{-7} mm^2 s^{-1} [39]
D_{Hl}	Diffusion coefficient of H ions in electrolyte	4.8×10^{-3} mm^2 s^{-1} [58,59]
L_{ϕ_c}	Interface kinetics coefficient	2×10^{-2} mm^2 N^{-1} s^{-1} [35]
m_{d}	Fracture model parameter	2.4 [31]
m_{c}	Corrosion model parameter	3 [31]
Λ	Hydrogen damage coefficient	0.7 [60]
ΔG^0_{b}	Gibbs free energy difference	3.2×10^4 J mol^{-1} [61]
$\bar{V}_{\mathrm{H}}$	Partial molar volume of H in Mg	2240 mm^3 mol^{-1} [62]
b	Evolution coefficient	1.7 [35]

hand, the y-displacement is fixed along the lower edge and the x-displacement is fixed along the left edge. Fig. 4(a) demonstrates the effect of hydrogen embrittlement on the development of the corrosion pit predicted by the computational simulations. The results clearly show that the reduction in the critical fracture energy caused by hydrogen atoms significantly accelerates the progression of pitting in the alloy substrate. After 5000 s of loading time, the crack depth shows a twofold increase when hydrogen embrittlement is considered. As illustrated in Fig. 4(b), the proceeding of the pit development closely follows the propagation of the crack with a significant accumulation of hydrogen atoms observed at the crack tip. Moreover, the hydrogen concentration at the crack tip increases notably under higher loadings.

The effects of environmental hydrogen concentration are demonstrated in Fig. 5. Fig. 5(a) and (b) show the crack depth evolution curve and stress corrosion crack growth rate vs. the loading time, respectively. It is revealed that higher environmental hydrogen concentrations result in significantly increased crack growth rates and earlier onsets of SCC. For instance, under the ambient hydrogen concentration of 0.3 wtppm, SCC occurs approximately 300 s earlier compared to the case with the concentration of 0.1 wtppm, and the final failure time of the sample is accelerated by about 600 s. However, the morphology of the pitting craters remains largely unchanged, as shown in Fig. 5(c). Furthermore, Fig. 5(b) shows that, under the current SSRT loading, SCC propagates at a relatively stable rate at the second stage, prior to final failure.

Fig. 6 illustrates the influence of the damage coefficient Λ in the model. A higher damage coefficient indicates the increased hydrogen embrittlement in the alloy matrix. As shown in Fig. 6(a)–(b), an increase in the damage coefficient results in an earlier onset of SCC and an accelerated crack growth rate. Specifically, when the damage coefficient increases from 0.5 to 0.9, the crack growth increase from 64 μm to 166 μm after the loading time of 4500 s as shown in Fig. 6(c). These results highlight the considerable influence of hydrogen embrittlement on the SCC behaviour of biodegradable magnesium alloys. Meanwhile, the ambient hydrogen concentration and the magnesium alloy's susceptibility to hydrogen embrittlement affect the crack growth under mechanical loadings.

3.2. Compact tension specimen: comparison with film rupture/dissolution/repassivation model

The SCC behaviour is associated with the film rupture/dissolution/repassivation mechanism [63]. As a result, the crack growth rate typically follows a power-law relationship with respect to the stress intensity factor K_{I}, as given by [64]:

$$\frac{da}{dt} = C_1 K_{\mathrm{I}}^{C_2}, \tag{86}$$

where C_1 and C_2 are material and environment-dependent constants. To evaluate the prediction consistency between the proposed model and the film rupture-dissolution-repassivation model, a compact tension (CT) specimen of the AZ91D magnesium alloy is employed to investigate the effect of K_{I} on the SCC crack growth rate. The simulation setup is illustrated in Fig. 7. The model is discretised using fully integrated second-order, 8-node plane strain elements with a mesh size of 0.04 mm. The model parameters are listed in Table 2. The plastic deformation behaviour is characterised using the multilinear isotropic hardening law with the parameters reported in [65]. The centre of the circular hole is connected to the hole edge via a distributed coupling. Throughout

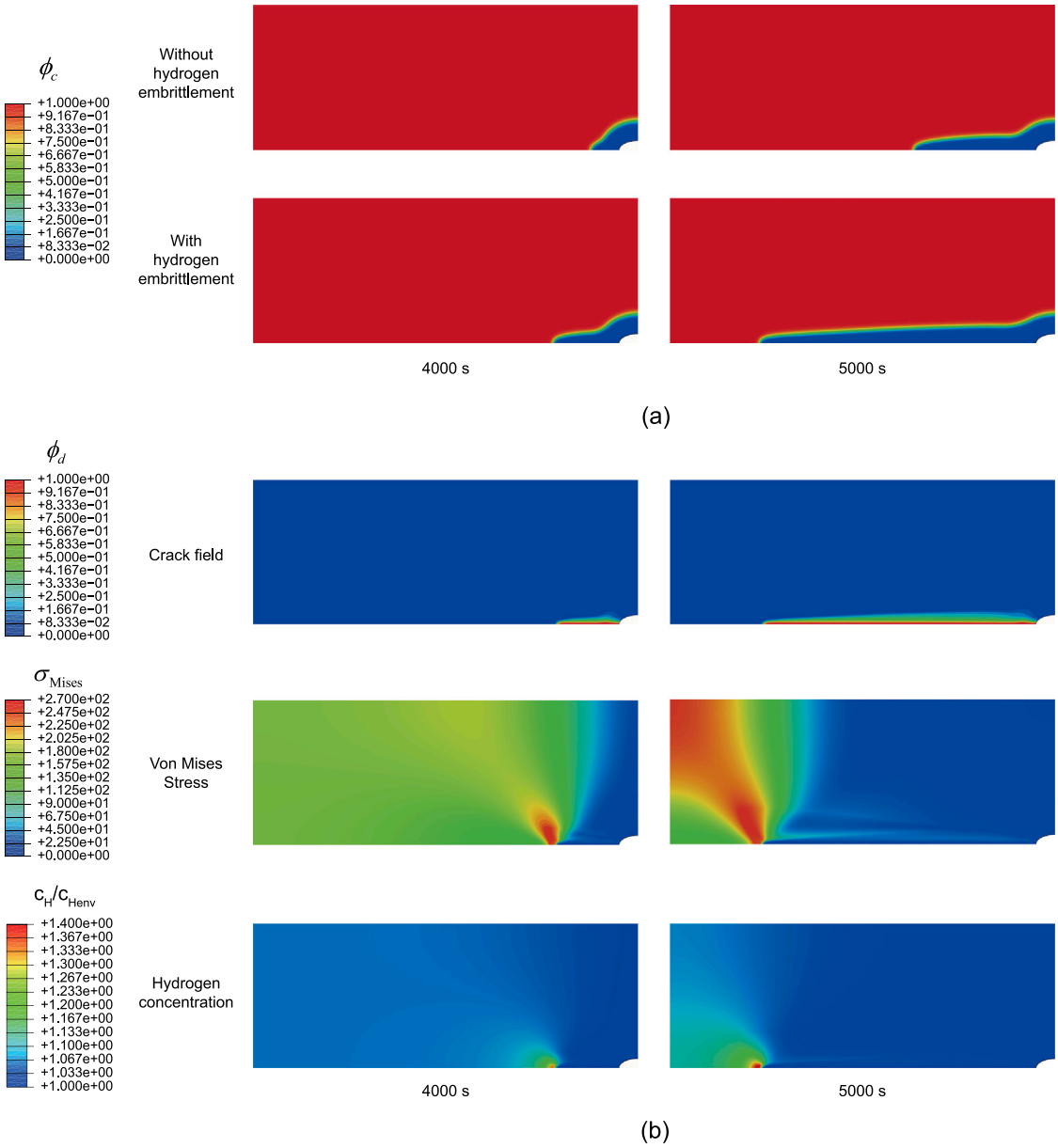

Fig. 4. Computational results of the notched plate. (a) Corrosion pit evolutions predicted by including and neglecting hydrogen-embrittlement at the loading time t = 4000 s and 5000 s. (b) Contour plots of the crack field, von Mises stress and the normalised hydrogen concentration predicted by considering hydrogen-embrittlement at the loading time t = 4000 s and 5000 s.

the simulation, a constant load is applied at this point, while its displacement in the x-direction is constrained. The initial and boundary conditions for chemical species are consistent with those described in Section 3.1.

In this computational example, the crack growth rate is quantified as the average propagation rate over the initial 200 μm extension of the SCC. The simulated crack growth rates under various values of K_I are presented in Fig. 8, while Fig. 9 illustrates the evolution of the SCC region under different loading conditions. The results demonstrate that the proposed model effectively capture the experimentally observed trends reported in [66]. To compare the present model with the classical film rupture-based model, a curve-fitting analysis was conducted on the simulation data. The fitted curve in Fig. 8 follows the equation:

$$\frac{da}{dt} = 5.589 \times 10^{-12} K_I^{2.278}, . \tag{87}$$

This result confirms that the predicted SCC growth rate exhibits a power-law dependence on K_I, consistent with the mechanistic trends described by classical film rupture-based models.

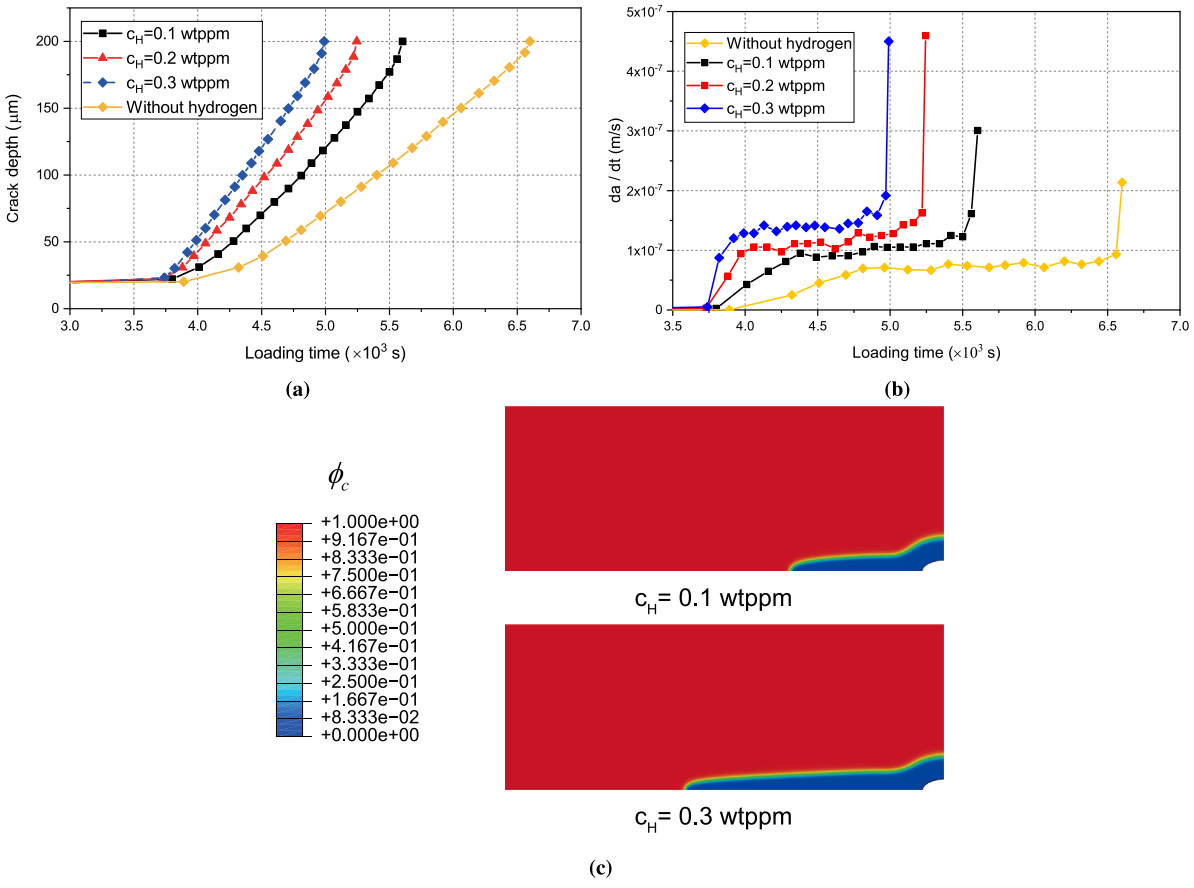

Fig. 5. Effect of the environmental hydrogen concentration on crack growth. (a) Crack depth-loading time curves, (b) crack growth rate ($\frac{da}{dt}$)-loading time curves and (c) corrosion interface morphologies at the loading time t = 4500 s.

Table 2
Model parameters of the magnesium alloy AZ91D.

Parameter	Physical interpretation	Value
$\bar{K}$	Effective bulk modulus	32 158 MPa [65]
$\bar{G}$	Effective shear constant	17 472 MPa [65]
$\bar{\sigma}_y$	Effective initial yield stress	88.28 MPa [65]
l_{d}	Fracture interface thickness	0.1 mm
g_{dm0}	Initial critical fracture energy	8.5 MPa mm
α_{c}	Gradient energy coefficient	2.04×10^{-3} N
w_{c}	Height of the double-well energy barrier	1.408 J mm^{-3}
D_{Mp}	Diffusion coefficient of Mg in corrosion product	3.5×10^{-7} mm^2 s^{-1} [31]
$L_{\phi_{\mathrm{c}}}$	Interface kinetics coefficient	1.2×10^{-6} mm^2 N^{-1} s^{-1}

3.3. PEO-coated sample: validation against in vitro experiments of biodegradable magnesium alloy WE43MEO

In order to validate the feasibility of the proposed model for the PEO-coated magnesium alloy WE43MEO, we consider a square plate with an initial flaw, illustrated in Fig. 10(a) and (b). The initial flaw in the alloy matrix is assumed to be a quarter-elliptical geometry with a width of 5 μm and a depth of 10 μm. The initial crack with a length of 40 μm is introduced in the barrier film with a thickness of 2 μm according to the suggested proportion of broken regions in the barrier film for matching the experimental data of *in vitro* corrosion tests in DMEM [35]. In addition, a representative 100 μm-wide section with the detailed porous microstructure of PEO coating is embedded in the plate as shown in Fig. 10(c). In the experiment, it was found that the coating has an average thickness of 20 μm, a porosity of 15.7%, and a mean pore radius of 1.3 μm [35]. Accordingly, the pore structure of the coating is represented by random pores with radii of 1 to 2 μm. For modelling initial defects in the PEO coating, a discharge channel with a width of 1 μm is aligned to connect the surface defect of the PEO coating and the initial flaw in the alloy matrix.

Experimental studies showed that the micropores connected by microcracks in the PEO coating act as microchannels for allowing the penetration of electrolytes to the alloy matrix, significantly affecting the SCC behaviour. The microdefects in the PEO coating

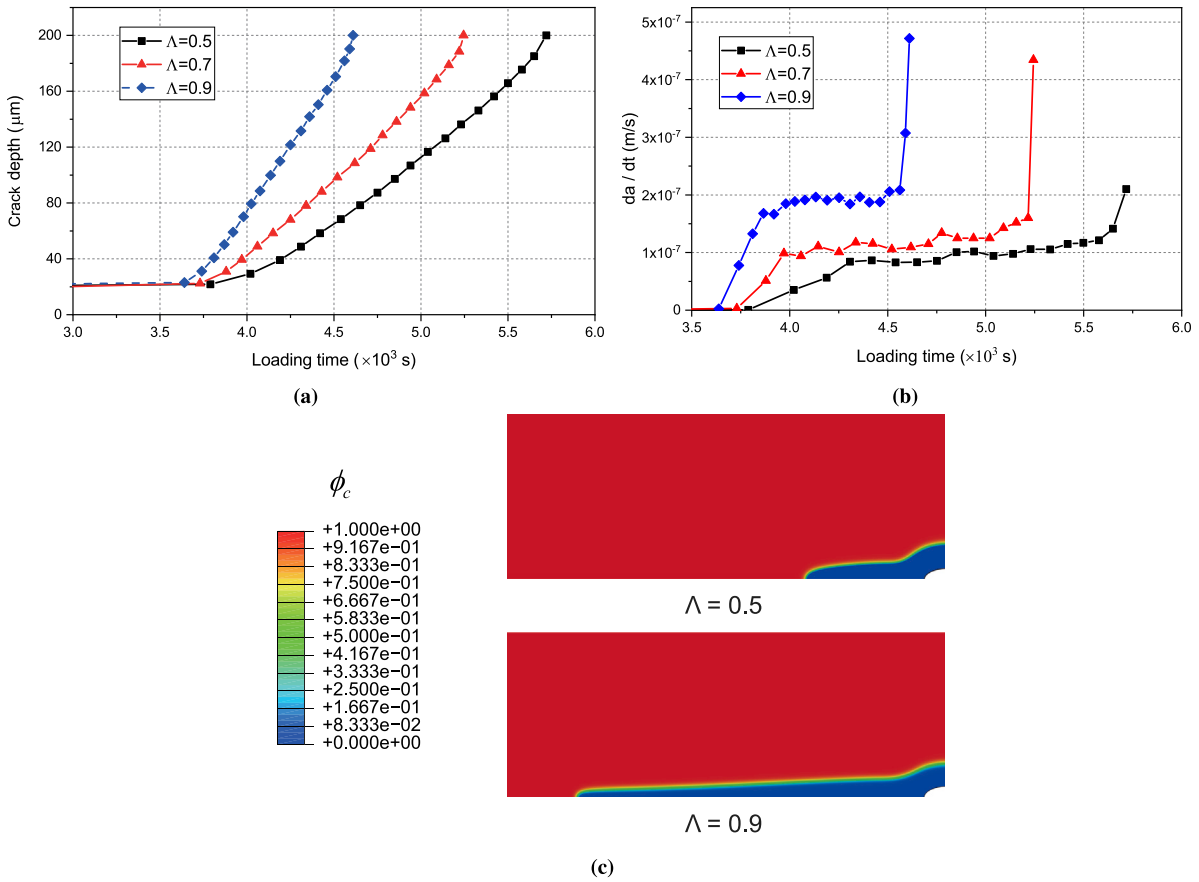

Fig. 6. Effect of the hydrogen damage coefficient Λ on crack growth. (a) Crack depth-loading time curves, (b) crack growth rate ($\frac{da}{dt}$)-loading time curves and (c) corrosion interface morphologies at the loading time t = 4500 s.

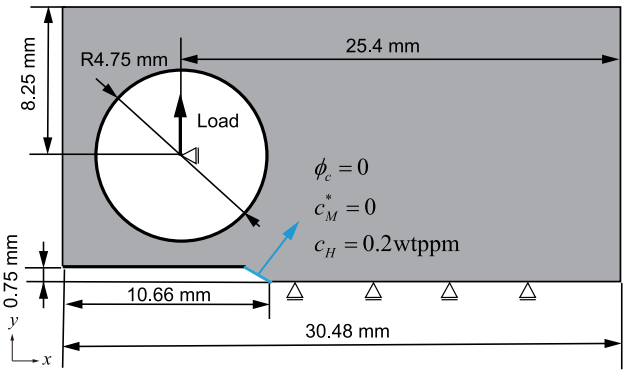

Fig. 7. Geometry and boundary conditions of the CT specimen.

are typically a few microns, and the embedded microcracks are often less than 1 μm in width [67]. It is still challenging to detect these defects using X-ray microcomputed tomography techniques. From the computational point of view, accurately capturing such 3D morphology of microdefects would require extremely fine meshing, resulting in prohibitively high computational costs for FEM simulations. Therefore, the PEO coating model is simplified with pre-defined microcracks and micropores to balance model fidelity with computational cost. The idealised initial cracks and defects in the coating are assumed to be filled with corrosive medium, which allows the diffusion of ions through these defects in the computational simulation. As a result, these defects can act as stress-corrosion initiation sites under chemomechanical loadings in the computational simulation.

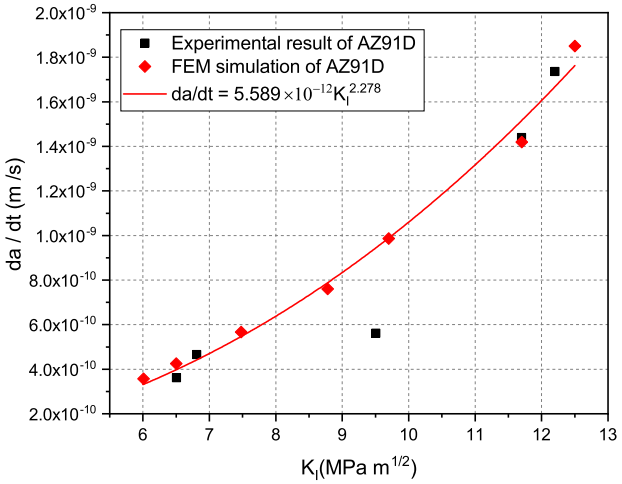

Fig. 8. Crack growth rate ($\frac{da}{dt}$) versus K_I for the magnesium alloy AZ91D from *in vitro* stress corrosion tests [66] and multiphysics phase-field simulations.

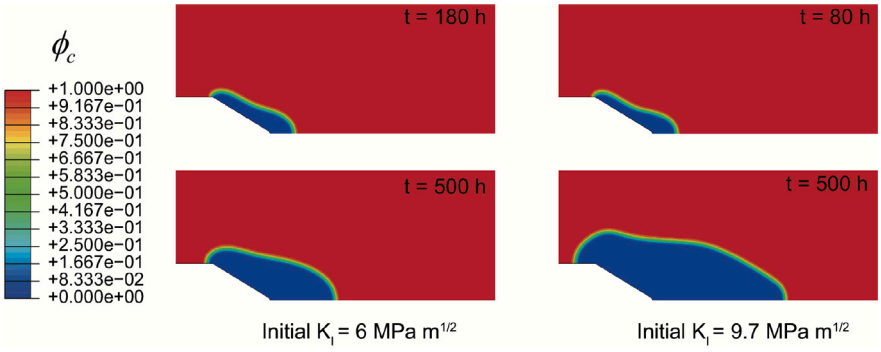

Fig. 9. Contour plots of the corrosion phase fields in the CT specimen under different static loadings.

Table 3
Material properties of the PEO coating.

Parameter	Physical interpretation	Value
$\tilde{K}$	Effective bulk modulus	173 913 MPa
$\tilde{G}$	Effective shear constant	94 488 MPa
g_{dm}	Critical fracture energy	4×10^{-4} MPa mm [31]
$D_{\mathrm{M\text{-}PEO}}$	Diffusion coefficient of Mg within PEO coating	8×10^{-10} mm^2 s^{-1} [35]
b	Evolution coefficient	1.7 [35]

The model is discretised using fully integrated second-order 8-node plane elements with a maximum mesh size of 0.5 μm in the alloy substrate and 0.2 μm in the PEO coating. The boundary conditions $c_{\mathrm{M}}^{*}=0$, $c_{\mathrm{H}}=0.16$ wtppm and $\phi=0$ are prescribed along the upper boundary immersed in the electrolyte, while the initial conditions are $c_{\mathrm{M}}^{*}=1$, $c_{\mathrm{H}}=0$ and $\phi_{\mathrm{c}}=1$ in the alloy matrix, and $c_{\mathrm{M}}^{*}=0$, $c_{\mathrm{H}}=0$ and $\phi_{\mathrm{c}}=0$ in the PEO coating. The environmental hydrogen concentration ($c_{\mathrm{H}}=0.16$ wtppm) is set to match physiological conditions, as referenced in [68]. The bottom edge is fixed in the y-direction, while the left edge is constrained in the x-direction. Moreover, it is assumed that the microstructural defects in the computational models are initially filled by electrolyte, which enables a fast diffusion of species. The model parameters of magnesium alloy WE43MEO used in the simulations is listed in Table 1. The properties of PEO coating are given in Table 3. The elastic modulus of coating is 240 GPa according to Gazenbiller's result [33] and the Poison ratio is assumed to take the same value of the alloy substrate. The critical fracture energy of the PEO coating is calibrated to have the tensile strength of MgO (96 MPa) [69]. For simplification, the diffusion coefficient of hydrogen in the PEO coating is assumed to be equivalent to that in the alloy substrate.

3.3.1. Corrosion tests

We first validate the simulation setup against the *in vitro* data reported in [16] by analysing the corrosion process without mechanical loading. The average corrosion depth in the experiments is evaluated according to the collected volume of hydrogen

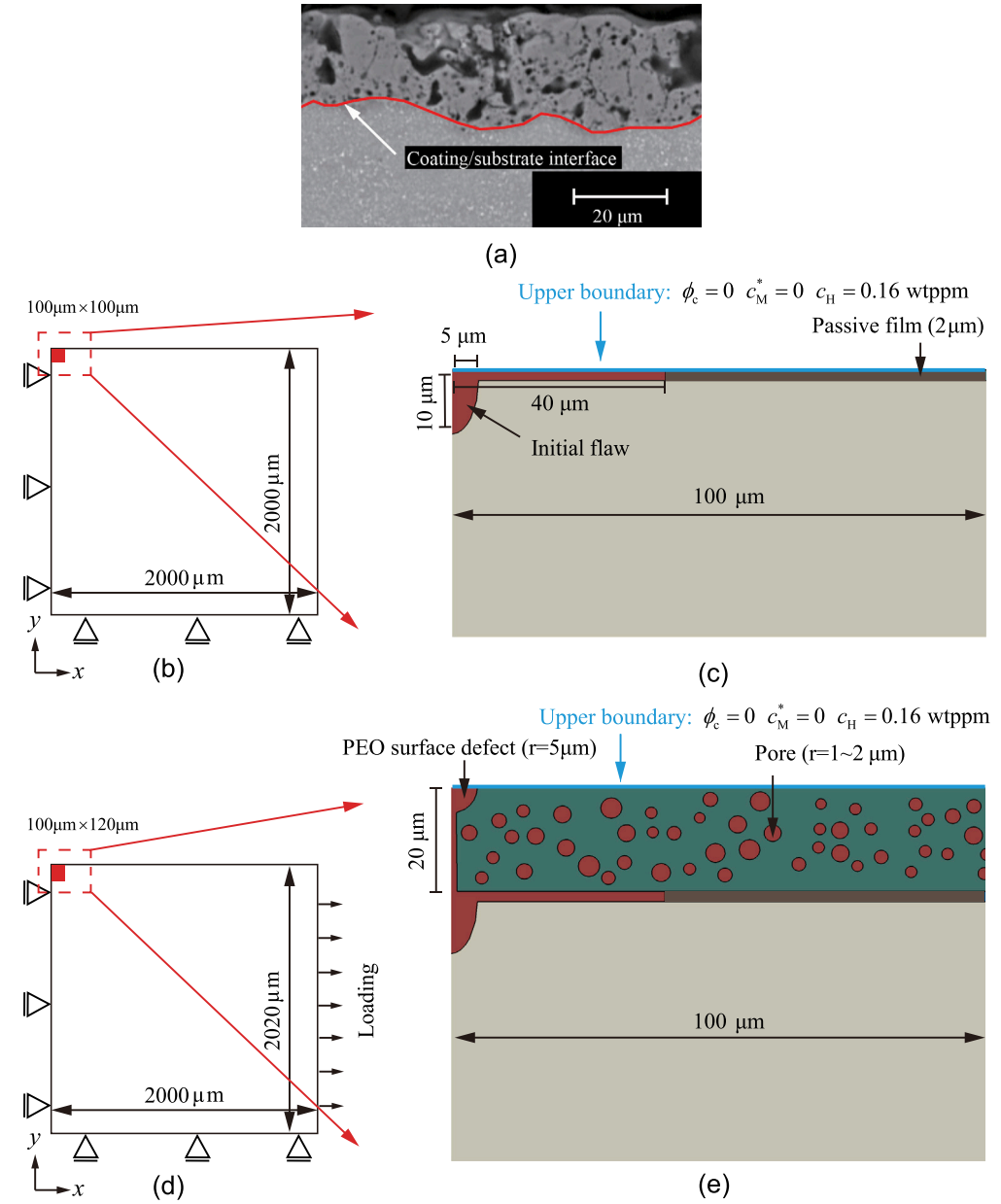

Fig. 10. (a) SEM image of the PEO coating. (b–e) Computational models and boundary conditions for non-coated and PEO-coated WE43MEO samples.

gas V_H (mL) following

$$CD_{Exp} = PM_{Mg}V_H/(\rho_{Mg}RTA_s) \tag{88}$$

with the gas pressure P (1 atm), the molar mass of magnesium M_{Mg} (24 310 mg mol^{-1}), the density of WE43MEO ρ_{Mg} (1840 mg cm^{-3}), the molar gas constant R (82.05 mL atm K^{-1} mol^{-1}), the test temperature T (310.15 K) and the surface area of specimen A_s (3.016 cm^2). The simulated average corrosion depth is calculated by dividing the corroded area A_c by the specimen width W_s

$$CD_{Sim} = A_c/W_s\,. \tag{89}$$

Figs. 11 and 12 illustrate the corrosion depth-time curves and the corresponding pitting morphology evolution for uncoated and coated magnesium alloys, respectively. In the initial stage of corrosion, the PEO coating has a negligible influence on the corrosion of the alloy substrate due to the existing microdefects, which enable the direct contact between the electrolyte and the alloy surface.

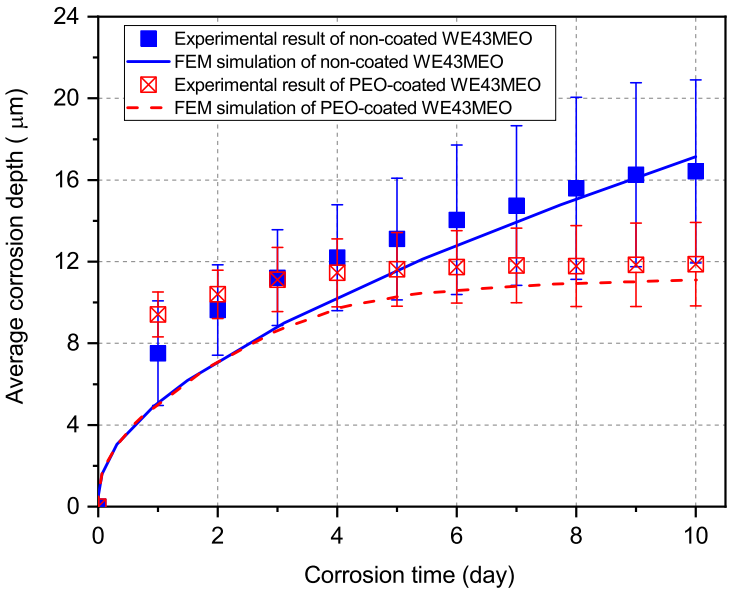

Fig. 11. The evolution of the average corrosion depth for the non-coated and PEO-coated WE43MEO from *in vitro* corrosion tests [16] and phase-field simulations.

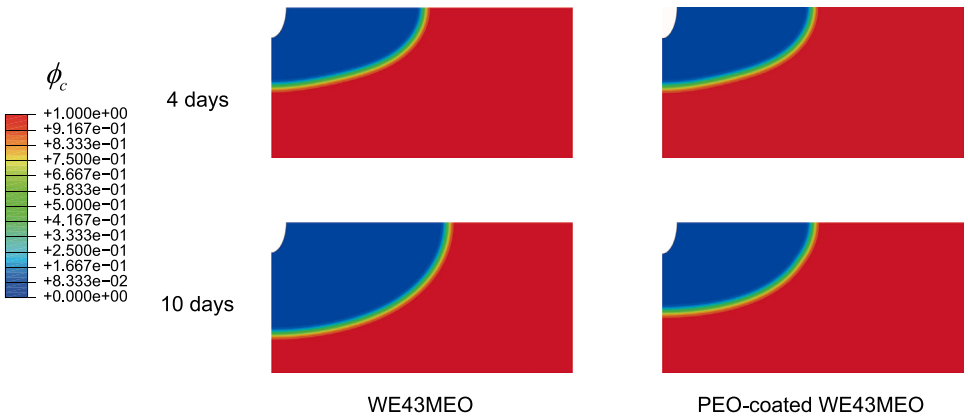

Fig. 12. Pit morphologies of the non-coated and PEO-coated WE43MEO after 4 days and 10 days.

However, as corrosion products accumulate in the microdefects of the PEO coating, the penetration of the solution is increasingly hindered, leading to the accumulation of Mg ions in the PEO coating, as illustrated in Fig. 13. In this circumstance, the corrosion rate of the coated specimen becomes significantly lower than that of the uncoated specimen after 4-day immersion. The good agreement between the experimental and computational results confirms the validity of the computational setup and the corrosion model's parameters for uncoated and coated WE43MEO.

3.3.2. Static loading-corrosion tests

Biodegradable implants are subjected to significant mechanical loadings *in vivo* conditions. Therefore, it is essential to investigate the influence of mechanical loading on the degradation behaviour of PEO-coated magnesium alloys. In previous experimental study in [22], static tensile stresses of 120 MPa, 180 MPa and 240 MPa (corresponding to 40%, 60% and 80% of ultimate tensile strength of WE43MEO) were used to analyse the loading effect on the corrosion behaviour of the PEO-coated WE43MEO immersed in DMEM. The experiments showed that the loading levels of 120 MPa and 180 MPa have only a minor effect on the corrosion process, whereas the tensile stress of 240 MPa markedly accelerated the corrosion process. Due to experimental limitations, the underlying mechanisms remain unclear. To gain deeper insight into the SCC behaviour of PEO-coated magnesium alloys, we conduct the simulation under these loading conditions. A constant surface traction is imposed on the right edge in the x-direction, the left edge is fixed in x-direction and the bottom edge is fixed in y-direction. The sample is then subject to the above mentioned chemomechanical boundary conditions for one day. The critical fracture energy of corrosion product here is calibrated to be 4.5% of the uncorroded material

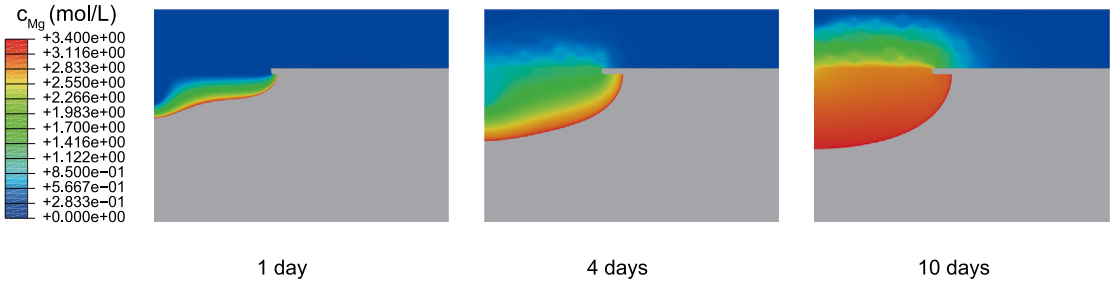

Fig. 13. The evolution of the Mg-concentration during the corrosion process of PEO-coated WE43MEO.

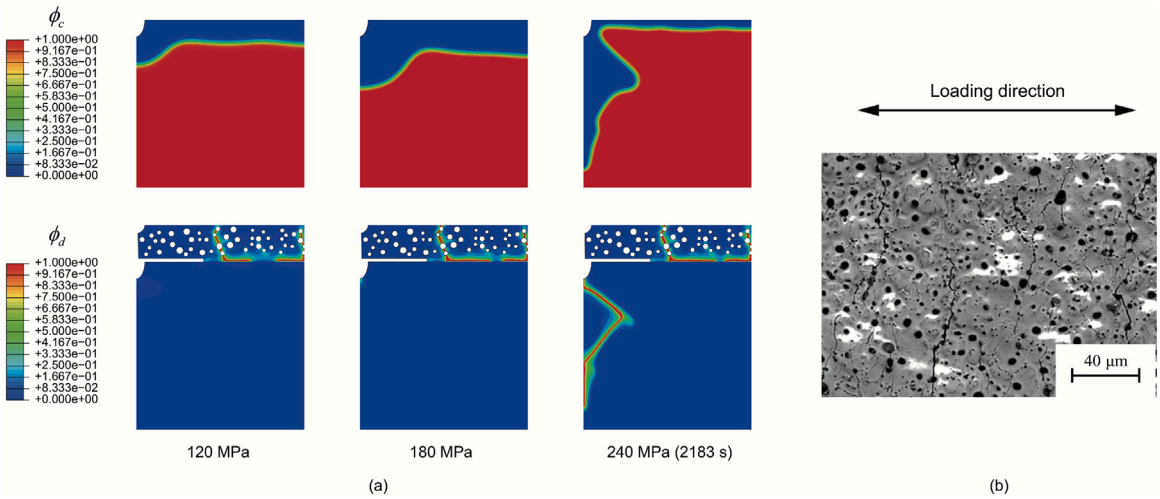

Fig. 14. (a) Pit morphologies and crack field distribution under static loadings with different stress levels over 1-day duration (2183 s for the loading case of 240 MPa). (b) The SEM image for the PEO coating surface with aligned microcracks of the failed specimen tested with the loading 240 MPa.

to reproduce the experimental results. Since the applied loads far exceed the load-bearing capacity of the PEO coating, the coating fractures entirely under all three load levels as shown in Fig. 14. A penetrating crack is visible, connecting multiple pores, and the interface between the coating and alloy substrate is nearly torn apart. These results indicate that the PEO coating does not protect the alloy substrate under high stress loadings. In the loading case of 120 MPa, although the PEO coating is completely fractured, there is minimal damage in corrosion products on the alloy substrate (see Fig. 14). After one day of corrosion, the corrosion pit reaches a depth of approximately 30 μm, which is obviously deeper than the case in the absence of mechanical loading. When the loading increase to 180 MPa, significant damage of corrosion products is observed near the initial flaw, further accelerating pit growth. In both cases, the fracture and delamination of the PEO coatings lead to the direct exposure of the alloy substrate to the corrosion medium, resulting in a significantly higher corrosion rate compared to pure corrosion conditions. However, the corrosion pits with the depth of several tens-microns after one day of exposure has a limited effect on the overall structural integrity of the specimen, which agrees with the experimental results as shown in Fig. 15, where the reduction of the mechanical integrity in our simulation results is calculated by the ratio of the maximum crack depth to the height of the square plate.

A further increase of the external loading to 240 MPa causes extensive damage of corrosion products, resulting in pronounced SCC phenomena. Due to numerical convergence limitations, only the results from the last successfully converged computational step are presented. Notably, a crack develops significantly within the alloy substrate, and its inclined orientation indicates localised plastic deformations. Under the combined influence of mechanical loading and corrosion, the SCC pit shows a clear tendency to expand downward. After 2183 s of corrosion, the crack depth reaches 89 μm. It is reported [22] that the SCC crack growth is driven by a hydrogen-assisted mechanism and proceeds slowly at the initial stage. As the crack propagates, local stress concentrations accelerate the crack growth until a final failure. Therefore, the specimen will fail completely within the corrosion time of one day according to the simulation result. Under high mechanical loadings, the SCC resistance of PEO-coated WE43MEO alloys in DMEM appears to depend mainly on the alloy substrate, while the coating's protective effect becomes negligible. The open discharge channel in the coating induce localised stress concentrations and facilitate the growth of the corrosion pit, whereas the coating's porous structure fractures readily under high stresses, and delamination at the coating–substrate interface eliminates the residual protection for the alloy substrate.

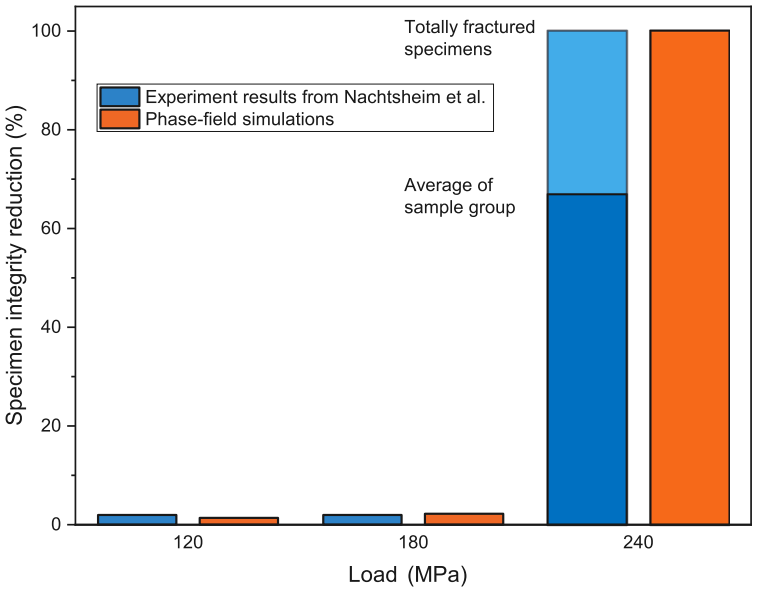

Fig. 15. The integrity reduction of PEO-coated specimens under static loadings with different stress levels over 1-day duration [22]. In the loading case of 240 MPa, two out of three specimens fractured completely after 1 day, while the third retained almost its original strength.

In this study, the hydrogen damage coefficient was estimated based on experimental observations of a notable reduction in material ductility after hydrogen charging, which ranges from 60% to 88% compared to the samples tested in air [70]. Furthermore, Winzer et al. [71] demonstrated that hydrogen pre-charged magnesium specimens exhibited a 68% drop in fracture toughness compared to uncharged counterparts. Based on these results, a hydrogen damage coefficient of 0.7 is adopted in the simulations to reflect this level of degradation. This parameter is considered to fall within a physically reasonable range for biodegradable Mg alloys. Fig. 16 demonstrates the prediction sensitivity to the hydrogen damage coefficient under the static loading of 240 MPa. After 500 s of the loading, SCC cracks initiated in all three cases with varying hydrogen damage coefficients. When the hydrogen damage coefficient was increased from 0.7 to 0.9, the SCC crack develops to an unstable propagation stage after 1200 s, indicating a significant acceleration in the SCC propagation. Similarly, the coefficient of 0.7 results in an approximately 30% longer SCC crack than that observed in the case of 0.5. These results suggest that the prediction of SCC crack growth rate is sensitive to the hydrogen damage coefficient, while the model captures the overall SCC behaviour. It is also worth noting that the degree of data scatter is inherent in the SCC experiments. Under a constant applied stress of 240 MPa, one specimen exhibited almost no visible cracking while two others fractured completely. Given such experimental scatter, the level of uncertainty introduced by estimating the hydrogen damage coefficient is considered as acceptable. Nevertheless, it is necessary to calibrate this parameter under in vitro conditions for more accurate predictions.Due to the complex chemo-mechanical coupling effects, the microscale validation for the degradation of biodegradable magnesium alloys is important but also technically challenging. In existing literature, hydrogen diffusion models in metals are typically validated by comparing the hydrogen permeation behaviour under controlled conditions [72,73]. Recent studies have shown that neutron imaging is a promising method for visualising hydrogen in magnesium alloys, with spatial resolution limited to several tens of micrometres [74,75]. In addition, atom probe tomography, secondary ion mass spectrometry, elastic recoil detection analysis and nuclear reaction analysis have been used to measure the hydrogen in metals. To understand the coupling mechanism of the SCC process, experimental efforts have been devoted to *in situ* experiments for dynamic monitoring of crack growth under chemo-mechanical environments involving simple corrosive media [76–78], such as quantifying local hydrogen concentration fields and crack kinetics. However, applying these methods to biodegradable magnesium alloys with high chemical activity requires significant experimental efforts and developments. The complex chemical compositions in DMEM, including multiple ions and organic components, lead to very complicated mechano-electrochemical processes of formation/rupture/dissolution of corrosion products as well as the adsorption of proteins to the specimen [79]. The complex chemo-mechanical environments make it technically difficult to conduct microscopic monitoring of the coupled degradation process of magnesium alloys under in vitro conditions. Hence, current study mainly focuses on the development of the modelling method rather than microscale experimental validation for the coupling mechanism.

3.4. Post-sealed PEO-coated sample without open defects: numerical studies on the SCC behaviour

Since open pores and discharge channels in the coatings significantly weaken its protective ability, a variety of post-treatments have been developed to seal these open pores and initial flaws, such as phosphate-based sealing treatment [80]. Here, we numerically investigate the SCC behaviour of such post-sealed PEO-coated samples under SSRT loading conditions using the proposed

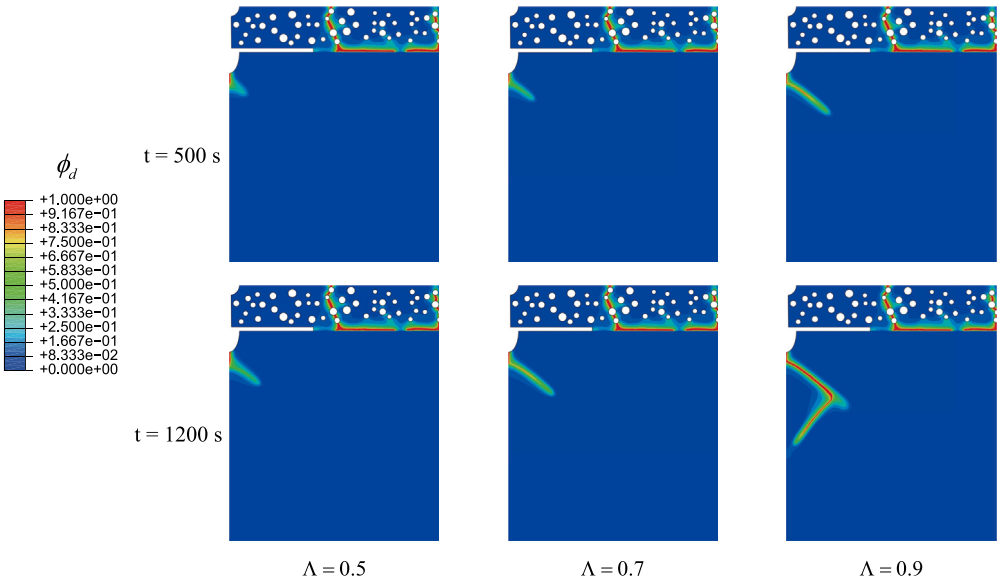

Fig. 16. Contour plots of the crack phase field under the static loading of 240 MPa with different hydrogen damage coefficients after 500 and 1200 s.

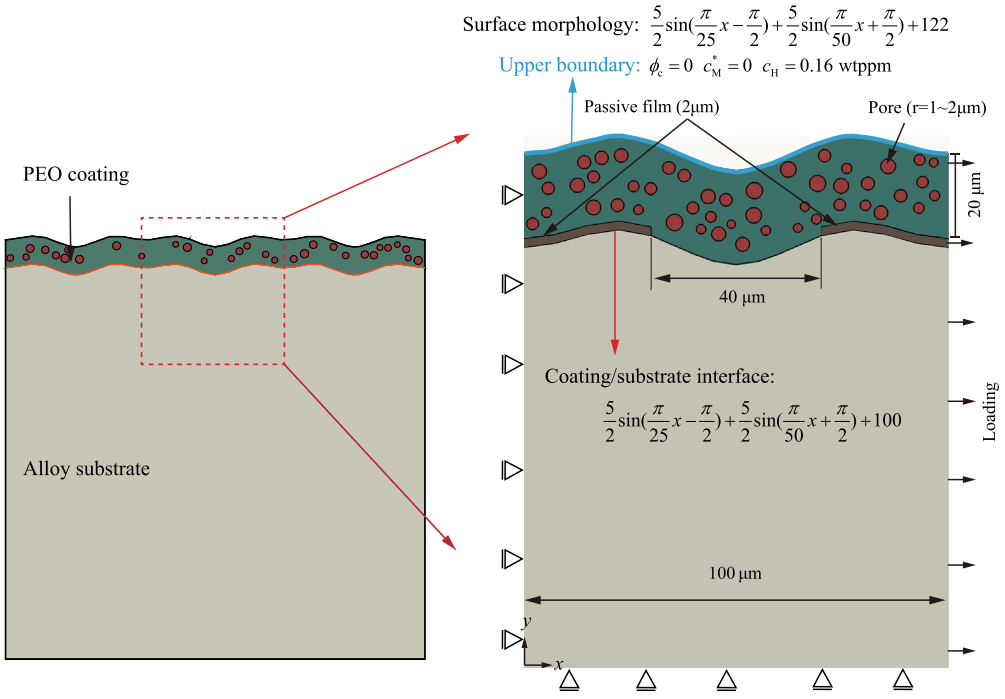

Fig. 17. The representative computational model and boundary conditions for the post-sealed PEO-coated sample without open defects. The origin of the coordinate system is located at the lower left corner of the model.

multiphysics model. Accordingly, a representative microstructural model without discharge channels and initial film cracks is employed for the computation simulations. The geometry and boundary conditions of the model are illustrated in Fig. 17. The surface roughness of the specimen is approximated using a sinusoidal function $\frac{R_i}{2}\sin(\frac{\pi}{25}x-\frac{\pi}{2})+\frac{R_i}{2}\sin(\frac{\pi}{50}x+\frac{\pi}{2})+100$ with $R_i=5$ being a roughness parameter, based on the following assumptions: (1) the interface wave height varies between 5 and 10 μm, and is not strictly uniform as shown in Fig. 10(a), and (2) the deepest troughs repeats approximately every 100 μm. This periodic profile triggers pronounced local stress concentrations under mechanical loadings. The porous structure of the coating is modelled

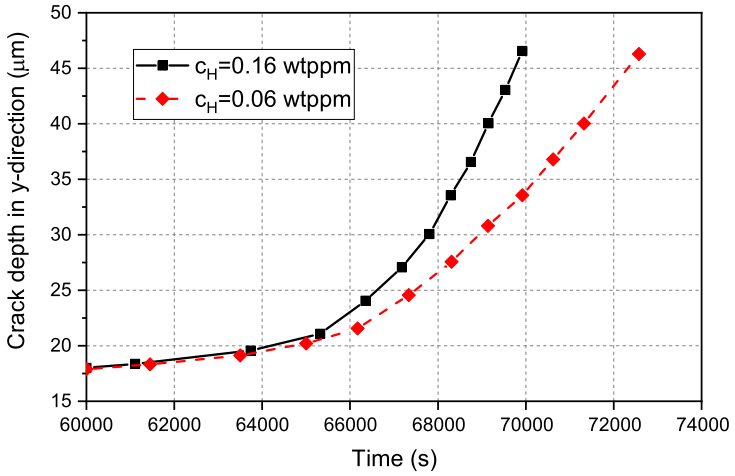

Fig. 18. Crack depth-loading time curves of the post-sealed PEO-coated sample under three different strain rates. The crack depth is the vertical distance between the pit front and the horizontal mid-point of the coating–substrate interface.

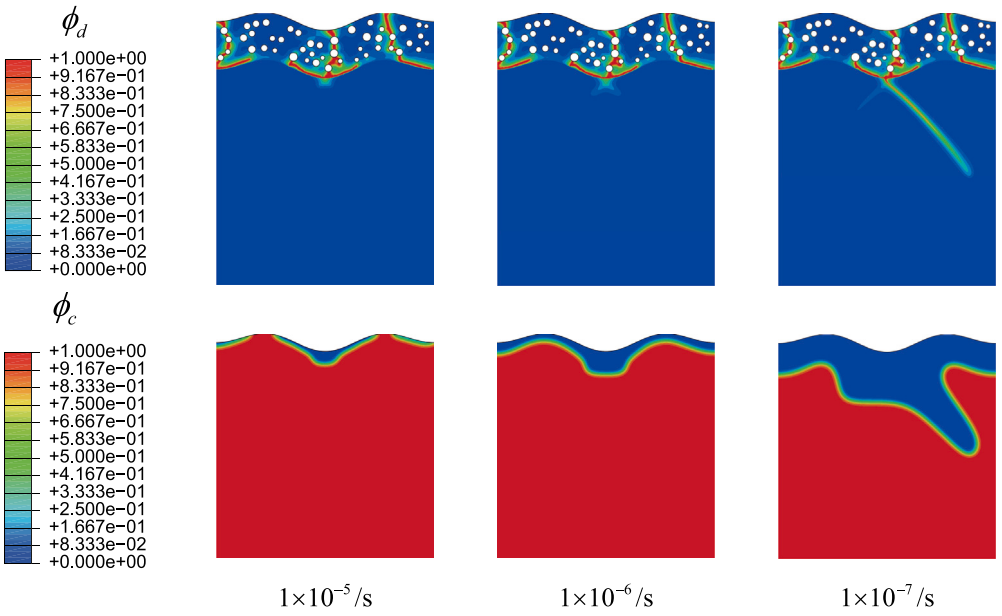

Fig. 19. Contour plots of the crack and corrosion phase fields at the global strain of 0.7% under different strain rates.

by randomly distributed circular pores with pore radii range from 1 to 2 μm, resulting in the porosity of approximately 15.7%. The model is discretised using fully integrated second-order 8-node plane strain elements with a maximum mesh size of 0.2 μm in the coating and 0.5 μm in the substrate. The boundary conditions $c_{\mathrm{M}}^{*}=0$, $c_{\mathrm{H}}=0.16$ wtppm and $\phi_{\mathrm{c}}=0$ are prescribed along the upper boundary, while the initial conditions are $c_{\mathrm{M}}^{*}=1$, $c_{\mathrm{H}}=0$ and $\phi_{\mathrm{c}}=1$ in the alloy matrix, and $c_{\mathrm{M}}^{*}=0$, $c_{\mathrm{H}}=0$ and $\phi_{\mathrm{c}}=0$ in the PEO coating. The bottom edge is fixed in the y-direction, while the left edge is constrained in the x-direction. A displacement in the x-direction is applied at the right edge with a constant slow loading rate.

Fig. 18 depicts the evolution of the vertical crack depth in coated samples tested with three loading rates. It is seen that the loading rate significantly affects the SCC response of the coated alloys due to the corrosion-fracture interaction. A lower loading rate leads to higher corrosion damage and thereby smaller deformations for the failure of the material. With the loading rate 1×10^{-7} s^{-1}, the vertical crack depth attains 45 μm at a global strain of 0.7% on the representative model of the microstructure, whereas the same crack depth is not reached until the global strain of 1.44% with the loading rate 1×10^{-5} s^{-1}. This behaviour can be attributed to the fact that the longer exposure time at lower strain rates allows more corrosion and hydrogen diffusion in the alloy substrate. Fig. 19 compares the crack field distribution and corrosion morphology of the samples at three strain rates when the global strain reaches 0.7%. We observe that the PEO coating is almost fractured. The fracture of PEO coatings causes significant

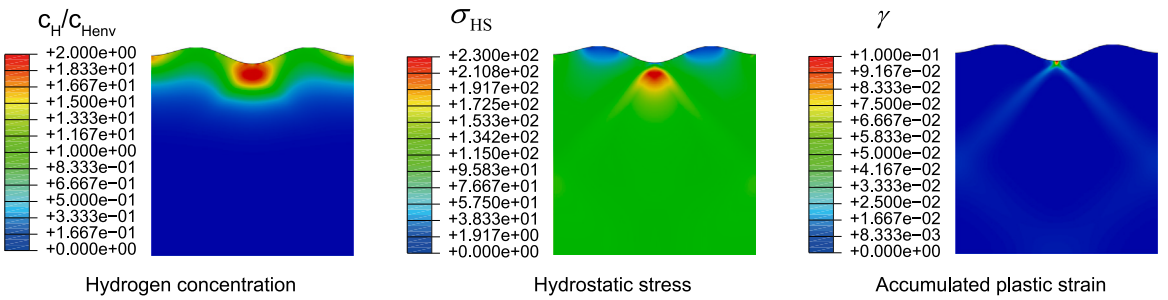

Fig. 20. Contour plots of the hydrogen distribution, the hydrostatic stress and the accumulated plastic strain in the alloy substrate at the global strain of 0.7% under the loading rate of 1×10^{-5} s^{-1}.

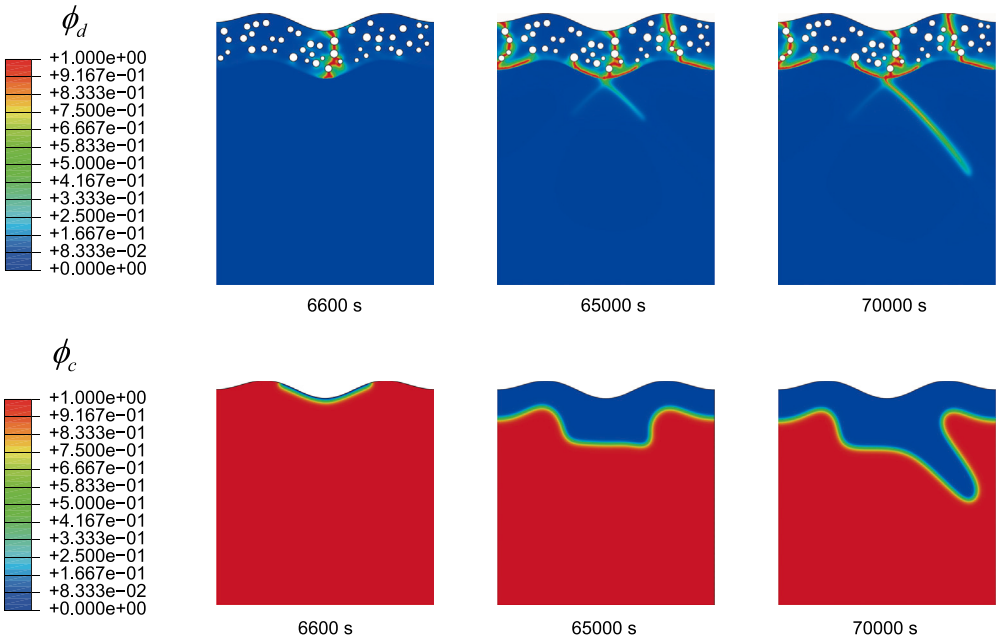

Fig. 21. Contour plots of the crack and corrosion phase fields in the coated sample with post sealing for the case of the loading rate 1×10^{-7} s^{-1} at the loading time t = 6600 s, 65 000 s and 70 000 s.

stress concentration and hydrogen enrichment near the coating-alloy interface as shown in Fig. 20. The localised concentration of hydrogen and accumulated plastic strain trigger stress corrosion cracking of the alloy substrate. Because of a longer immersion time, the evidence of stress corrosion is more apparent in the case of the loading rate 1×10^{-7}.

Fig. 21 shows the distribution of crack and corrosion fields after 6600 s, 65 000 s and 70 000 s in the case of the loading rate of 1×10^{-7} s^{-1}. At the loading time of 6600 s, a through-coating crack has formed, triggering the initiation of pit and the local hydrogen enrichment, yet the intact portions of the coating and barrier film still shield most of the surface. The continued straining to 65 000 s causes interfacial delaminations and additional penetrating cracks, eliminating the coating's protective function. The damage in corrosion products further accelerates the corrosion process, leading to failure after 70 000 s.

To investigate the influence of the environmental hydrogen concentration on the SCC behaviour, we compared the SCC response under two representative hydrogen exposure levels: 0.16 wtppm and 0.06 wtppm. The elevated hydrogen concentration (0.16 wtppm) corresponds to the condition within the bone marrow cavity, while the lower exposure level (0.06 wtppm) reflects subcutaneous tissue environments [68]. As shown in Fig. 22, the simulation results clearly demonstrate that the stress corrosion cracking rates at the elevated hydrogen exposure in bone marrow increase dramatically compared to the subcutaneous-level scenario. At 70 000 s, the pitting depth of the Mg alloy substrate in the bone marrow cavity environment is 38.7% deeper than that observed under subcutaneous exposure. This quantitative comparison shows that a higher environmental hydrogen concentration significantly enhances the SCC susceptibility. To better understand the influence of microstructural features of PEO coatings on the SCC process, a static loading of 40 MPa is applied to the right side of the model to observe the SCC behaviour. To quantify the damage in the alloy substrate, the average corrosion depth is defined as the total corroded area divided by the sample width of 100 μm. The effects of coating porosity and coating/substrate roughness are investigated as follows:

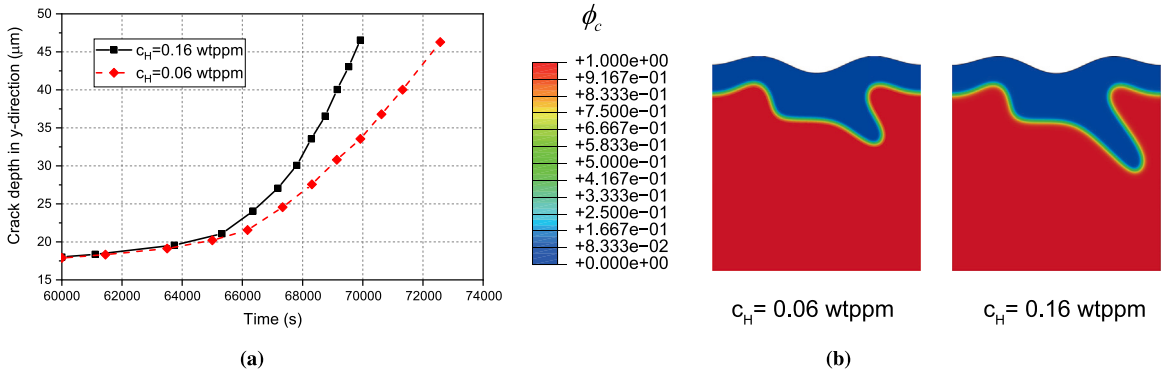

Fig. 22. Effect of the environmental hydrogen concentration on crack growth in the coated sample with post sealing for the case of the loading rate 1×10^{-7} s^{-1}. (a) Crack depth-loading time curves and (b) corrosion interface morphologies at the loading time t = 70 000 s. The crack depth is the vertical distance between the pit front and the horizontal mid-point of the coating–substrate interface.

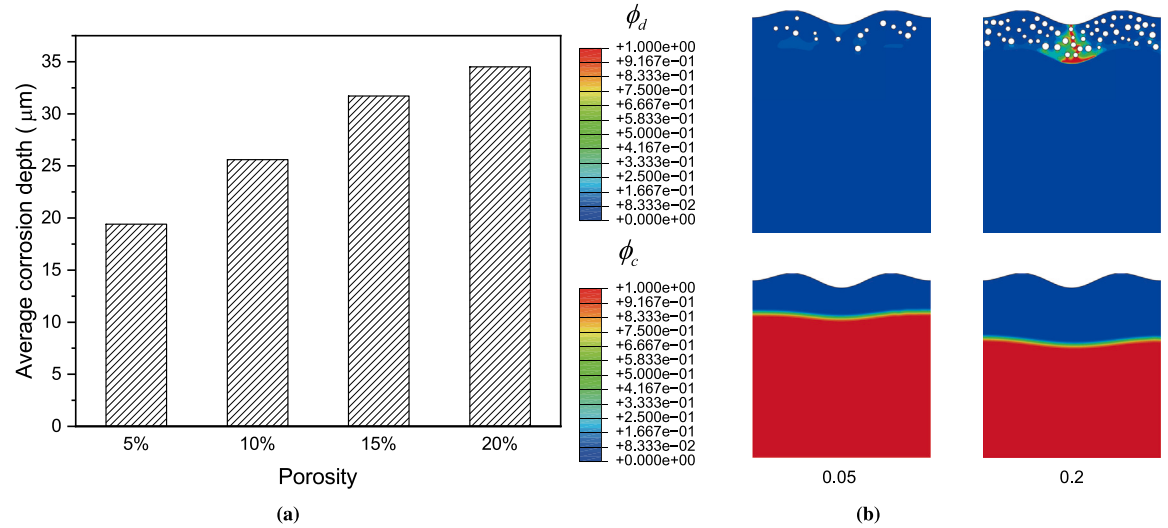

Fig. 23. Effect of the coating porosity. (a) The influence of the coating porosity on average corrosion depth after 4 days and (b) contour plots of the crack and corrosion phase fields after 4 days for different porosities of PEO coatings.

(i) **The influence of porosity.** The coating thickness is fixed at 20 μm, and the roughness parameter is set to 5 μm. The porosity of the coatings varied from 0.05 to 0.20 with the increment of 0.05. The corresponding average stress-corrosion depths after 4 days were 19.4, 25.6, 31.7, and 34.5 μm, respectively, as shown in Fig. 23(a). It is evident that increasing porosity results in higher corrosion susceptibility of the coated magnesium alloys under static external loadings. Under the static loading of 40 MPa, coatings with the lower porosity exhibit less damage, as shown in Fig. 23(b).

(ii) **The influence of roughness.** The coating thickness is fixed at 20 μm, and the porosity is set to 0.15. Two coatings with roughness parameters of 2 and 5 are compared. The corresponding average stress-corrosion depths after 4 days are 20 and 31.7 μm, respectively, as shown in Fig. 24(a). As illustrated in Fig. 24(b), a smoother interface can effectively mitigate coating damage caused by stress concentration, thereby enhancing the protective performance of the coating under low static loadings.

4. Conclusions

In this study, we have developed a multiphysics phase-field model for the micromechanical analysis of the SCC behaviour of PEO-coated biodegradable magnesium alloys. The model developed within the thermodynamically consistent framework captures the coupled interactions among corrosion, fracture, and hydrogen diffusion. Different numerical examples at the microscale were used to demonstrate the predictive ability of the SCC behaviour of magnesium alloys with different coatings under various loading conditions. Based on the computational results, the following conclusions can be drawn:

- The proposed phase-field modelling approach provides a quantitative method for evaluating the corrosion and damage behaviour of PEO-coated magnesium alloys. The validation of computational results with in vitro corrosion and SCC

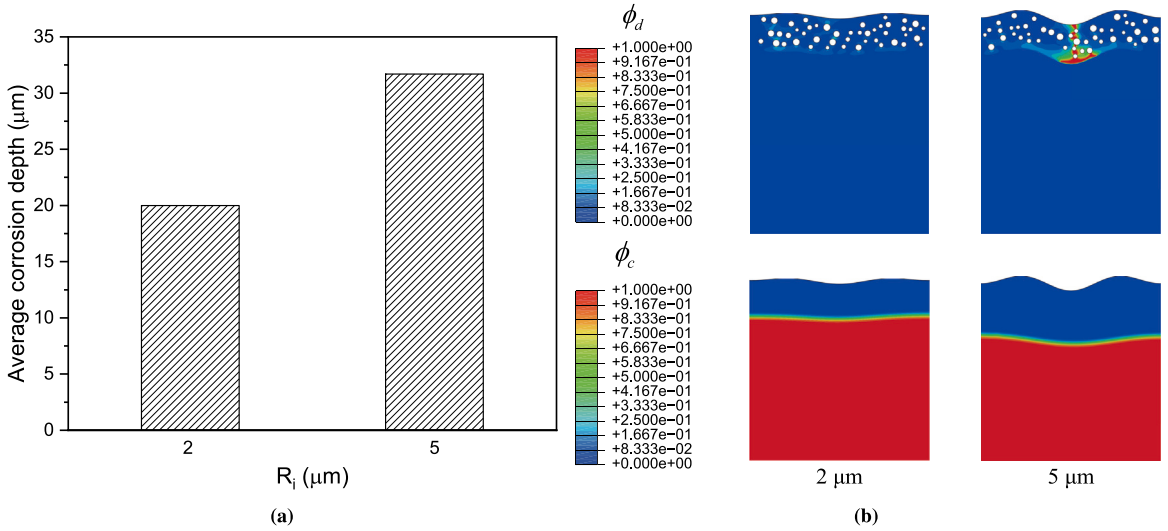

Fig. 24. Effect of the coating/substrate roughness. (a) The influence of the coating/substrate interface roughness on the average corrosion depth after 4 days and (b) contour plots of the crack and corrosion phase fields after 4 days for different coating/substrate interface roughness.

experiments confirm that the model reasonably reproduces the variation of the corrosion rate under immersion tests and the SCC behaviour under constant loadings.

- Hydrogen-rich environments markedly accelerate SCC in magnesium alloys. Simulation results indicate that an ambient hydrogen concentration of 0.3 wtppm leads to a 50% increase in the SCC growth rate under SSRT loadings compared to that under 0.1 wtppm. Additionally, the intrinsic susceptibility of magnesium alloys to hydrogen embrittlement plays a crucial role in determining the SCC growth rate. When the hydrogen damage coefficient Λ increases from 0.5 to 0.9, the steady-state SCC growth rate under SSRT loadings approximately doubles.
- The computational results demonstrate that cracking in the coating and interfacial delamination generate pronounced stress concentrations within the alloy substrate, facilitating hydrogen accumulation at the crack tip. In the simulation, localised plastic deformations near the crack tip serve as the primary driving force for crack propagation due to the coupling term ζ_{pd} in the proposed model, and further promotes the evolution of pitting corrosion via the coupling term ζ_{dc} and diffusion coupling function h_{f}.
- Micro-defects within the coating act as stress concentrators, initiating early-stage cracking. Lower porosity and smoother interfaces in PEO coatings significantly enhance their fracture strength, thereby improving their resistance to corrosion under moderate static loading conditions. Specifically, a coating with 5% porosity exhibits a 43.7% smaller corrosion rate compared with that of 20% porosity under the static loading of 40 MPa, while reducing the interface roughness parameter R_{i} from 5 μm to 2 μm decreases the corrosion rate by 36.9% under 40 MPa loadings.
- The used numerical examples demonstrates the reasonable predictive ability of the proposed multiphysics phase-field model for describing the SCC behaviour of PEO-coated biodegradable magnesium alloys under chemo-mechanical loadings, which is crucial for *in silico* design and evaluation of the mechanical integrity of magnesium implants in physiological environments.

Under the physiological conditions, cyclic or variable amplitude loadings can significantly affect the initiation and propagation of SCC in biomedical magnesium alloys. These complex loading scenarios require corresponding experimental studies and a more sophisticated refinement of the proposed model, which need to be considered in future studies to enhance the applicability and robustness of the computational model.

CRediT authorship contribution statement

Dawei Zhang: Writing – original draft, Software, Investigation, Data curation, Conceptualization. **Songyun Ma:** Writing – review & editing, Supervision, Project administration, Methodology, Funding acquisition, Conceptualization. **Cheng Luo:** Writing – review & editing, Methodology, Investigation. **Huang Yuan:** Writing – review & editing, Methodology. **Bernd Markert:** Writing – review & editing, Supervision.

Declaration of competing interest

The authors declare that they have no known competing financial interests or personal relationships that could have appeared to influence the work reported in this paper.

Acknowledgements

This research was supported by the Federal Ministry of Education and Research of Germany in the framework of RePlaSys (project number FKZ 13GW0352B), and the China Scholarship Council (CSC) (Reference No. 202108080318).

Data availability

Data will be made available on request.

References

[1] Chakraborty Banerjee Parama, Al-Saadi Saad, Choudhary Lokesh, Harandi Shervin Eslami, Singh Raman. Magnesium implants: Prospects and challenges. Mater (Basel Switz) 2019;12(1).
[2] Narayanan TSN Sankara, Park Il Song, Lee Min Ho. Strategies to improve the corrosion resistance of microarc oxidation (MAO) coated magnesium alloys for degradable implants: Prospects and challenges. Prog Mater Sci 2014;60:1–71.
[3] Fouladi M, Amadeh A. Effect of phosphating time and temperature on microstructure and corrosion behavior of magnesium phosphate coating. Electrochim Acta 2013;106:1–12.
[4] Wong Hoi Man, Yeung Kelvin WK, Lam Kin On, Tam Vivian, Chu Paul K, Luk Keith DK, Cheung Kenneth MC. A biodegradable polymer-based coating to control the performance of magnesium alloy orthopaedic implants. Biomaterials 2010;31(8):2084–96.
[5] Moreno Lara, Mohedano Marta, Arrabal Raul, Matykina Endzhe. Development and screening of (Ca-P-Si-F)-PEO coatings for biodegradability control of Mg-Zn-Ca alloys. J Magnes Alloy 2022;10(8):2220–37.
[6] Chen Chi-An, Jian Shun-Yi, Lu Chia-Hsin, Lee Chia-Yu, Aktuğ Salim Levent, Ger Ming-Der. Evaluation of microstructural effects on corrosion behavior of AZ31B magnesium alloy with a MAO coating and electroless Ni-P plating. J Mater Res Technol 2020;9(6):13902–13.
[7] Srinivasan P Bala, Blawert C, Dietzel W, Kainer KU. Stress corrosion cracking behaviour of a surface-modified magnesium alloy. Scr Mater 2008;59(1):43–6.
[8] Song RG, Blawert C, Dietzel W, Atrens A. A study on stress corrosion cracking and hydrogen embrittlement of AZ31 magnesium alloy. Mater Sci Eng: A 2005;399(1–2):308–17.
[9] Winzer Nicholas, Atrens Andrej, Song Guangling, Ghali Edward, Dietzel Wolfgang, Kainer Karl Ulrich, Hort Norbert, Blawert Carsten. A critical review of the stress corrosion cracking (SCC) of magnesium alloys. Adv Eng Mater 2005;7(8):659–93.
[10] Tuchscheerer F, Krüger L. Hydrogen-induced embrittlement of fine-grained twin-roll cast AZ31 in distilled water and NaCl solutions. J Mater Sci 2015;50:5104–13.
[11] Jiang Jiahao, Geng Xue, Zhang Xiaobo. Stress corrosion cracking of magnesium alloys: A review. J Magnes Alloy 2023.
[12] Jafari Sajjad, Harandi Shervin Eslami, Singh Raman RK. A review of stress-corrosion cracking and corrosion fatigue of magnesium alloys for biodegradable implant applications. Jom 2015;67(5):1143–53.
[13] Choudhary Lokesh, Raman RK Singh, Hofstetter Joelle, Uggowitzer Peter J. In-vitro characterization of stress corrosion cracking of aluminium-free magnesium alloys for temporary bio-implant applications. Mater Sci Eng: C 2014;42:629–36.
[14] Gu Yanhong, Bandopadhyay Sukumar, Chen Cheng-fu, Ning Chengyun, Guo Yuanjun. Long-term corrosion inhibition mechanism of microarc oxidation coated AZ31 Mg alloys for biomedical applications. Mater Des (1980-2015) 2013;46:66–75.
[15] Cui Lan-Yue, Zeng Rong-Chang, Guan Shao-Kang, Qi Wei-Chen, Zhang Fen, Li Shuo-Qi, Han En-Hou. Degradation mechanism of micro-arc oxidation coatings on biodegradable Mg-Ca alloys: The influence of porosity. J Alloys Compd 2017;695:2464–76.
[16] Nachtsheim Julia, Ma Songyun, Burja Jaka, Batič Barbara Šetina, Markert Bernd. Tuning the long-term corrosion behaviour of biodegradable WE43 magnesium alloy by PEO coating. Surf Coat Technol 2023;474:130115.
[17] Srinivasan P Bala, Blawert C, Dietzel W. Effect of plasma electrolytic oxidation coating on the stress corrosion cracking behaviour of wrought AZ61 magnesium alloy. Corros Sci 2008;50(8):2415–8.
[18] Srinivasan P Bala, Blawert C, Dietzel W. Effect of plasma electrolytic oxidation treatment on the corrosion and stress corrosion cracking behaviour of AM50 magnesium alloy. Mater Sci Eng: A 2008;494(1–2):401–6.
[19] Xiong Ying, Shen Yongshui, He Liuyong, Yang Zengyuan, Song Renguo. Stress corrosion cracking behavior of LSP/MAO treated magnesium alloy during SSRT in a simulated body fluid. J Alloys Compd 2020;822:153707.
[20] He Xiuli, Liang Hongyu, Yan Zhifeng, Bai Rui. Stress corrosion cracking behavior of micro-arc oxidized AZ31 alloy. Proc Inst Mech Eng Part C: J Mech Eng Sci 2020;234(8):1640–52.
[21] Daavari Morteza, Conde Ana, Atapour Masoud, HosseinpourRokni Mohsen, Sánchez Hugo Mora, Mohedano Marta, Matykina Endzhe, Arrabal Raul. In vitro corrosion-assisted cracking of AZ31B Mg alloy with a hybrid PEO+ MWCNTs/PCL coating. Surf Interfaces 2023;42:103446.
[22] Nachtsheim Julia, Ma Songyun, Burja Jaka, Markert Bernd. In vitro evaluation of stress corrosion cracking susceptibility of PEO-coated rare-earth magnesium alloy WE43. Surf Coat Technol 2024;477:130391.
[23] Gastaldi Dario, Sassi V, Petrini Lorenza, Vedani Maurizio, Trasatti S, Migliavacca Francesco. Continuum damage model for bioresorbable magnesium alloy devices—Application to coronary stents. J Mech Behav Biomed Mater 2011;4(3):352–65.
[24] Ma Songyun, Yuan Huang. Computational investigation of multi-axial damage modeling for porous sintered metals with experimental verification. Eng Fract Mech 2015;149:89–110.
[25] Ma Songyun, Scheider Ingo, Bargmann Swantje. Anisotropic constitutive model incorporating multiple damage mechanisms for multiscale simulation of dental enamel. J Mech Behav Biomed Mater 2016;62:515–33.
[26] De Meo Dennj, Diyaroglu Cagan, Zhu Ning, Oterkus Erkan, Siddiq M Amir. Modelling of stress-corrosion cracking by using peridynamics. Int J Hydrog Energy 2016;41(15):6593–609.
[27] Chen Ziguang, Jafarzadeh Siavash, Zhao Jiangming, Bobaru Florin. A coupled mechano-chemical peridynamic model for pit-to-crack transition in stress-corrosion cracking. J Mech Phys Solids 2021;146:104203.
[28] Jafarzadeh Siavash, Chen Ziguang, Bobaru Florin. Computational modeling of pitting corrosion. Corros Rev 2019;37(5):419–39.
[29] Xie Chao, Bai Shijie, Liu Xiao, Zhang Minghua, Du Jianke. Stress-corrosion coupled damage localization induced by secondary phases in bio-degradable Mg alloys: phase-field modeling. J Magnes Alloy 2022.
[30] Kovacevic Sasa, Ali Wahaaj, Martínez-Pañeda Emilio, LLorca Javier. Phase-field modeling of pitting and mechanically-assisted corrosion of Mg alloys for biomedical applications. Acta Biomater 2023;164:641–58.
[31] Zhang Dawei, Ma Songyun, Nachtsheim Julia, Zhang Shunqi, Markert Bernd. A variational phase-field framework for multiphysics modelling of degradation and stress corrosion cracking in biodegradable magnesium alloys. J Mech Phys Solids 2024;190:105694.
[32] Němcová Aneta, Skeldon Peter, Thompson GE, Morse Stuart, Čížek Jan, Pacal Bohumil. Influence of plasma electrolytic oxidation on fatigue performance of AZ61 magnesium alloy. Corros Sci 2014;82:58–66.

[33] Gazenbiller Eugen, Mansoor Sohail, Konchakova Natalia, Serdechnova Maria, Zheludkevich Mikhail L, Blawert Carsten, Höche Daniel. Computational damage modelling of PEO coated extruded magnesium tested in slow strain rate configuration. Surf Coat Technol 2022;446:128758.
[34] van Gaalen Kerstin, Quinn Conall, Weiler Marek, Gremse Felix, Benn Felix, McHugh Peter E, Vaughan Ted J, Kopp Alexander. Predicting localised corrosion and mechanical performance of a PEO surface modified rare earth magnesium alloy for implant use through in-silico modelling. Bioact Mater 2023;26:437–51.
[35] Ma Songyun, Zhang Dawei, Zhang Peilei, Markert Bernd. Rapid prediction of the corrosion behaviour of coated biodegradable magnesium alloys using phase field simulation and machine learning. Comput Mater Sci 2025.
[36] Natishan PM, O'grady WE. Chloride ion interactions with oxide-covered aluminum leading to pitting corrosion: a review. J Electrochem Soc 2014;161(9):C421.
[37] Yang Junjie, Blawert Carsten, Lamaka Sviatlana V, Snihirova Darya, Lu Xiaopeng, Di Shichun, Zheludkevich Mikhail L. Corrosion protection properties of inhibitor containing hybrid PEO-epoxy coating on magnesium. Corros Sci 2018;140:99–110.
[38] Ascencio M, Pekguleryuz M, Omanovic SJCS. An investigation of the corrosion mechanisms of WE43 Mg alloy in a modified simulated body fluid solution: The influence of immersion time. Corros Sci 2014;87:489–503.
[39] Kappes Mariano, Iannuzzi Mariano, Carranza Ricardo M. Hydrogen embrittlement of magnesium and magnesium alloys: a review. J Electrochem Soc 2013;160(4):C168.
[40] Huang Chuanshi, Gao Xiaosheng. Phase field modeling of hydrogen embrittlement. Int J Hydrog Energy 2020;45(38):20053–68.
[41] Liang Y, Sofronis P, Aravas N. On the effect of hydrogen on plastic instabilities in metals. Acta Mater 2003;51(9):2717–30.
[42] Winzer N, Atrens A, Dietzel W, Song G, Kainer KU. Evaluation of the delayed hydride cracking mechanism for transgranular stress corrosion cracking of magnesium alloys. Mater Sci Eng: A 2007;466(1–2):18–31.
[43] Anand Lallit. A Cahn–Hilliard-type theory for species diffusion coupled with large elastic–plastic deformations. J Mech Phys Solids 2012;60(12):1983–2002.
[44] Amor Hanen, Marigo Jean-Jacques, Maurini Corrado. Regularized formulation of the variational brittle fracture with unilateral contact: Numerical experiments. J Mech Phys Solids 2009;57(8):1209–29.
[45] Cahn John W, Hilliard John E. Free energy of a nonuniform system. I. Interfacial free energy. J Chem Phys 1958;28(2):258–67.
[46] Kim Seong Gyoon, Kim Won Tae, Suzuki Toshio. Phase-field model for binary alloys. Phys Rev E 1999;60(6):7186.
[47] Mai Weijie, Soghrati Soheil, Buchheit Rudolph G. A phase field model for simulating the pitting corrosion. Corros Sci 2016;110:157–66.
[48] Anand Lallit, Mao Yunwei, Talamini Brandon. On modeling fracture of ferritic steels due to hydrogen embrittlement. J Mech Phys Solids 2019;122:280–314.
[49] Miehe C, Teichtmeister S, Aldakheel F. Phase-field modelling of ductile fracture: a variational gradient-extended plasticity-damage theory and its micromorphic regularization. Philos Trans R Soc A: Math, Phys Eng Sci 2016;374(2066):20150170.
[50] Alessi Roberto, Marigo Jean-Jacques, Maurini Corrado, Vidoli Stefano. Coupling damage and plasticity for a phase-field regularisation of brittle, cohesive and ductile fracture: one-dimensional examples. Int J Mech Sci 2018;149:559–76.
[51] Kristensen Philip K, Niordson Christian F, Martínez-Pañeda Emilio. A phase field model for elastic-gradient-plastic solids undergoing hydrogen embrittlement. J Mech Phys Solids 2020;143:104093.
[52] Kuhn Charlotte, Schlüter Alexander, Müller Ralf. On degradation functions in phase field fracture models. Comput Mater Sci 2015;108:374–84.
[53] Karma Alain, Kessler David A, Levine Herbert. Phase-field model of mode III dynamic fracture. Phys Rev Lett 2001;87(4):045501.
[54] Dittmann M, Aldakheel F, Schulte J, Wriggers P, Hesch. Variational phase-field formulation of non-linear ductile fracture. Comput Methods Appl Mech Engrg 2018;342:71–94.
[55] Borden Michael J, Hughes Thomas JR, Landis Chad M, Anvari Amin, Lee Isaac J. A phase-field formulation for fracture in ductile materials: Finite deformation balance law derivation, plastic degradation, and stress triaxiality effects. Comput Methods Appl Mech Engrg 2016;312:130–66.
[56] Wu Tao, De Lorenzis Laura. A phase-field approach to fracture coupled with diffusion. Comput Methods Appl Mech Engrg 2016;312:196–223.
[57] Hirth John P. Effects of hydrogen on the properties of iron and steel. Met Trans 1980;11:861–90.
[58] Ferrell RT, Himmelblau DM. Diffusion coefficients of hydrogen and helium in water. AIChE J 1967;13(4):702–8.
[59] AbuAisha Murad, Billiotte Joel. A discussion on hydrogen migration in rock salt for tight underground storage with an insight into a laboratory setup. J Energy Storage 2021;38:102589.
[60] Huang Zhifeng, Nie Jian-Feng. Interaction between hydrogen and solute atoms in {101 2} twin boundary and its impact on boundary cohesion in magnesium. Acta Mater 2021;214:117009.
[61] Kamilyan M, Silverstein R, Eliezer D. Hydrogen trapping and hydrogen embrittlement of Mg alloys. J Mater Sci 2017;52:11091–100.
[62] Baldi Andrea, Gonzalez-Silveira Marta, Palmisano V, Dam B, Griessen R. Destabilization of the Mg-H system through elastic constraints. Phys Rev Lett 2009;102(22):226102.
[63] Cui Chuanjie, Ma Rujin, Martínez-Pañeda Emilio. A generalised, multi-phase-field theory for dissolution-driven stress corrosion cracking and hydrogen embrittlement. J Mech Phys Solids 2022;166:104951.
[64] Mai Weijie, Soghrati Soheil. A phase field model for simulating the stress corrosion cracking initiated from pits. Corros Sci 2017;125:87–98.
[65] Murariu Mihai-Alin, Rusu Lucian, Belgiu George, Serban Dan-Andrei. Behaviour of AZ91 magnesium alloy in tension and torsion: experimental investigations and numerical modelling. In: IOP conference series: materials science and engineering. vol. 1319, IOP Publishing; 2024, 012014.
[66] Choudhary Lokesh, Raman RK Singh. Magnesium alloys as body implants: Fracture mechanism under dynamic and static loadings in a physiological environment. Acta Biomater 2012;8(2):916–23.
[67] Clyne Trevor William, Troughton Samuel Christopher. A review of recent work on discharge characteristics during plasma electrolytic oxidation of various metals. Int Mater Rev 2019;64(3):127–62.
[68] Zhao Daoli, Brown Andrew, Wang Tingting, Yoshizawa Sayuri, Sfeir Charles, Heineman William R. In vivo quantification of hydrogen gas concentration in bone marrow surrounding magnesium fracture fixation hardware using an electrochemical hydrogen gas sensor. Acta Biomater 2018;73:559–66.
[69] Nobre José, Ahmed Hawreen, Bravo Miguel, Evangelista Luís, De Brito Jorge. Magnesia (MgO) production and characterization, and its influence on the performance of cementitious materials: A review. Materials 2020;13(21):4752.
[70] Casajús Paula, Winzer Nicholas. Intergranular stress corrosion crack propagation in hot-rolled AZ31 Mg alloy sheet. Mater Sci Eng: A 2014;602:58–67.
[71] Winzer N, Atrens A, Dietzel W, Raja VS, Song G, Kainer KU. Characterisation of stress corrosion cracking (SCC) of Mg–Al alloys. Mater Sci Eng: A 2008;488(1–2):339–51.
[72] Kürten Dominik, Khader Iyas, Kailer Andreas. Determining the effective hydrogen diffusion coefficient in 100Cr6. Mater Corros 2020;71(6):918–23.
[73] Vecchi Lorenzo, Simillion Hans, Montoya Rodrigo, Van Laethem Dries, Van den Eeckhout Emilie, Verbeken Kim, Terryn Herman, Deconinck Johan, Van Ingelgem Yves. Modelling of hydrogen permeation experiments in iron alloys: Characterization of the accessible parameters–Part II–The exit side. Electrochim Acta 2018;262:153–61.
[74] Kumar Richi, Solís Cecilia, Trtik Pavel, Kriele Armin, Limberg Wolfgang, Wieland DC Florian, Moosmann Julian, Serdechnova Maria, Blawert Carsten, Ebel Thomas, et al. Characterizing effects of hydrogen ingress in Ti–Mg based hybrid implant materials. RSC Adv 2025;15(6):4472–80.
[75] Karimi Fahim, Börries Stefan, Pranzas P Klaus, Metz Oliver, Hoell Armin, Gizer Gökhan, Puszkiel Julián A, Riglos Maria VC, Pistidda Claudio, Dornheim Martin, et al. Characterization of LiBH4–MgH2 reactive hydride composite system with scattering and imaging methods using neutron and synchrotron radiation. Adv Eng Mater 2021;23(11):2100294.
[76] Kovac Jaka, Alaux Carole, Marrow T James, Govekar Edvard, Legat Andraz. Correlations of electrochemical noise, acoustic emission and complementary monitoring techniques during intergranular stress-corrosion cracking of austenitic stainless steel. Corros Sci 2010;52(6):2015–25.

[77] Bolivar J, Fregonese Marion, Réthoré Julien, Duret-Thual Claude, Combrade P. Evaluation of multiple stress corrosion crack interactions by in-situ digital image correlation. Corros Sci 2017;128:120–9.
[78] Zhao Pengxiong, Wu Wei, Ma Zeyu, Dan Yong. In situ study on the effect of stress on corrosion behavior of AZ91 magnesium alloy. Anti Corros Methods Mater 2022;69(2):204–13.
[79] Liu Chenglong, Xin Yunchang, Tian Xiubo, Chu Paul K. Degradation susceptibility of surgical magnesium alloy in artificial biological fluid containing albumin. J Mater Res 2007;22(7):1806–14.
[80] Qian Kun, Zhang Yue, Dong Qiangsheng, Shao Yi, Cheng Zhaojun, Ju Jia, Xue Feng, Chu Chenglin, Xia Dandan, Bai Jing. Enhancement of corrosion resistance and antibacterial properties of PEO coated AZ91D Mg alloy by copper-and phosphate-based sealing treatment. Corros Sci 2023;219:111218.